Appendix F: Ecology

F-4A Tappan Zee Bridge Construction Hydroacoustic Noise Modeling

Tappan Zee Bridge Construction Hydroacoustic Noise Modeling

Final report

Submitted to:
AECOM
One World Financial Center
200 Liberty St, 25th Floor
New York, NY 10281

Authors:
Alexander MacGillivray
Graham Warner
Roberto Racca
Caitlin O'Neill

March 2011
P001116-001
Version 1.0

JASCO Applied Sciences
Suite 2101, 4464 Markham St.
Victoria, BC, V8Z 7X8, Canada
Phone: +1.250.483.3300
Fax: +1.250.483.3301
www.jasco.com

Contents

Tables

Figures

1. Introduction

This report presents results of a hydroacoustic modeling study of construction noise from the proposed Tappan Zee Bridge/I-287 Corridor Project (the Project). This modeling study has been carried out by JASCO Applied Sciences (JASCO) in support of the Project's Environmental Impact Statement (EIS), to estimate the underwater range-of-influence of noise from pile driving activities. The sound level estimates from this modeling study are expressed, in terms of metrics, locations, environment and presentation, so as to be most readily amenable to assessments of potential biological impacts primarily on fish populations. Interpretation of such impacts is outside the scope of the present work.

The spatial distribution of noise has been analyzed for 24 construction scenarios, encompassing seven unique pile driving locations, four different piles sizes, and five different acoustic metrics including acoustic particle velocity. In addition, noise mitigation resulting from the application of best management practices (BMPs) has been modeled. The modeling has considered two distinct time scales: noise exposure over the brief duration of a single pile driving hammer strike and the cumulative exposure over a full day of construction activity. Model scenarios have been developed to cover two possible bridge designs (single level and dual level). The model scenarios have been developed in cooperation with the Project engineering team to ensure an accurate representation of the activities that will be carried out during construction of the proposed bridge.

Underwater noise levels have been modeled using three different sound propagation modeling codes (MONM, VSTACK, and FWRAM), all of which have been developed by JASCO. These three codes apply different numerical algorithms for modeling underwater sound propagation (parabolic equation, wavenumber integration, Fourier synthesis), and each has a different domain of validity. They have been used in combination to generate the various acoustic metrics that are required for assessing noise impacts on aquatic resources in the Hudson River. All of the models employed in the current study fully account for the frequency composition of the source signal and the physics of acoustic propagation in the water and underlying geological substrates.

The seven modeling locations considered (Figure 1) span the entire bridge crossing and are representative of the distinctive sound propagation regimes among the pile driving scenarios in the overall construction plan. The pile size modeled at each location is appropriate to that particular segment of the bridge span. Site-specific representations of the geoacoustic properties of the underlying substrates have been modeled at each of the seven modeling locations. Acoustic footprints resulting from simultaneous pile driving at multiple locations have been modeled for both proposed bridge designs, and individual footprints have been modeled for four of the seven locations. Lastly, the effect of applying Best Management Practices to reduce acoustic emissions has been estimated at all seven pile driving locations. Modeling results are presented in a variety of complementary formats including planar maps of the sound level maximized over the full depth of the water column, plots of sound level versus range along single transects, and graphs of the frequency content of the sound at a set of sample locations.

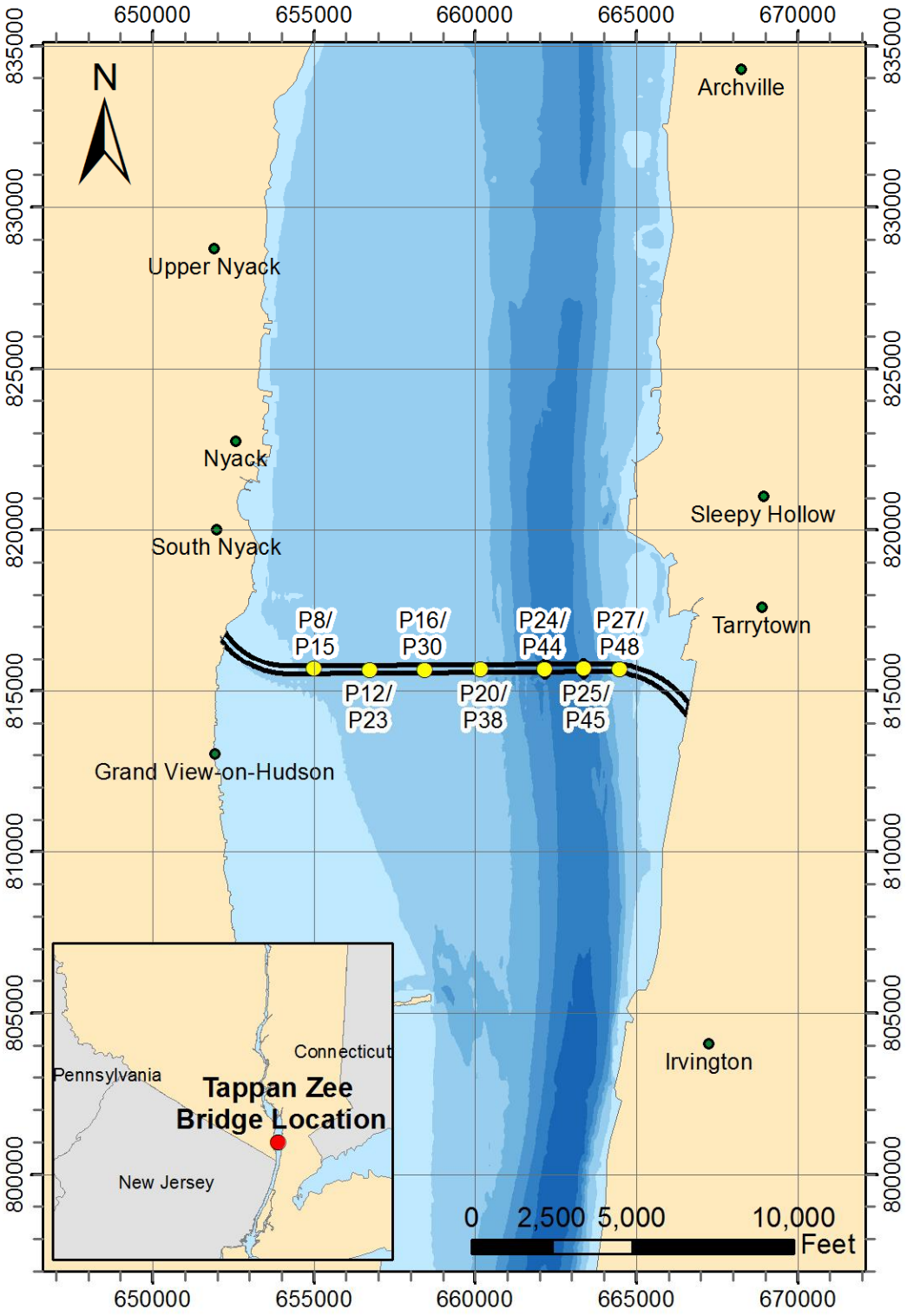

Figure 1. Location of proposed Tappan Zee Bridge and pile driving modeling locations (yellow dots). Annotations indicate construction pier numbers (dual level/single level) corresponding to each modeling location. Map coordinates are New York State Plane East (feet). Inset shows the location of the proposed bridge project.

2. Acoustics Background

2.1. Acoustics Terminology

Sound is the result of mechanical vibration waves traveling through a fluid medium such as air or water. These vibration waves generate a time-varying pressure disturbance that oscillates above and below the ambient pressure. Sound waves may be perceived by the auditory system of an animal, or they may be measured using an acoustic sensor (a microphone or hydrophone). Water conducts sound four times faster than air due to its lower compressibility; the speed of sound travelling in water is approximately 4900 ft/s. Sound is used extensively by marine organisms for communication and for learning about their environment. Humans may use sound purposely to probe the marine environment through technologies like sonar; more often, human activities such as marine construction generate underwater noise as an unintended side-effect.

Sources of underwater sound may be mechanical (e.g., a ship), biological (e.g., a whale) or environmental (e.g., rain). Noise, in general parlance, refers to unwanted sound that may affect humans or animals. Noise at relatively low levels can form a background that interferes with the detection of other sounds; at higher levels noise can also be disruptive or harmful. Common sources of naturally occurring underwater environmental noise include wind, rain, waves, seismic disturbances and vocalizations of marine fauna. Anthropogenic (i.e., man-made) sources of underwater noise include marine transportation, construction, geophysical surveys and sonar. Underwater noise usually exhibits both spatial and temporal variation.

2.2. Properties of Sound

The fundamental properties of sound waves are frequency, amplitude, wavelength, and intensity. Frequency, f, is the rate of pressure oscillation, per unit time, of a sound wave. Amplitude, A, is the maximum absolute pressure deviation of a sound wave. If c is the speed of sound in a medium, then the pressure disturbance due to a plane harmonic sound wave (Figure 2), at time t and location x, may described by the following expression:

$$P(x,t) = A\cos\left(2\pi f\left(x/c - t\right)\right) \tag{1}$$

The wavelength, λ, is the distance travelled by a sound wave over one complete cycle of oscillation. For plane harmonic sound waves, wavelength is equal to the frequency divided by the speed of sound:

$$\lambda = f/c \tag{2}$$

Harmonic waves are of fundamental importance in acoustics due to a well known mathematical law (Fourier's theorem) which states that any arbitrary waveform can be represented by the superposition of harmonic waves.

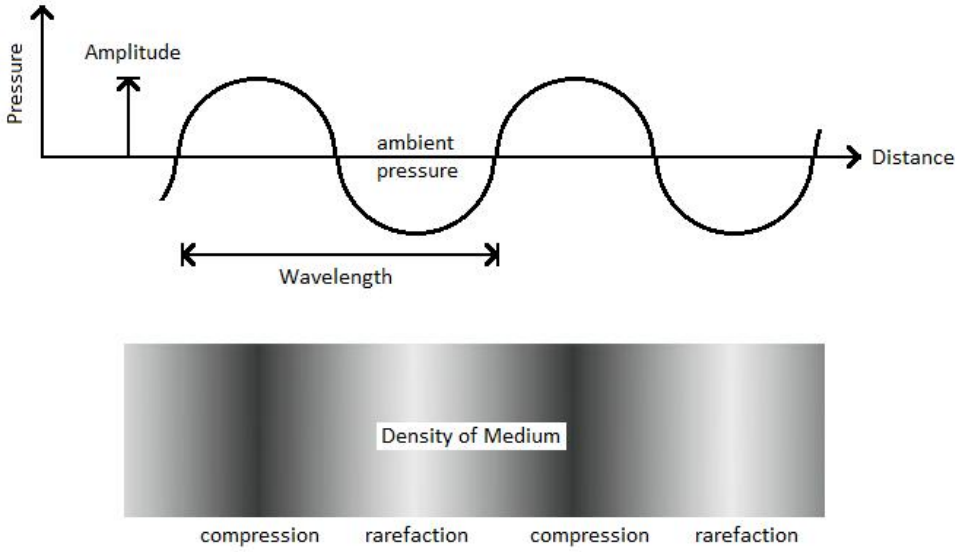

Figure 2: A snapshot of the pressure disturbance due to a plane harmonic sound wave.

Intensity is the acoustic power, per unit area, carried by a travelling sound wave. In general, intensity is related to the amplitude of a sound wave, but it also depends on the compressibility and density of the acoustic medium. The loudness of a sound is related to its intensity; however, loudness is a subjective term that refers to the perception of sound intensity, rather than the actual intensity itself. For humans and other animals, loudness also depends on the frequency and duration of sound.

2.3. Acoustic Metrics

Sound pressure and intensity are most commonly measured on the decibel (dB) scale. The dB scale is a logarithmic scale that expresses a quantity relative to a predefined reference level. Sound pressure, in dB, is expressed in terms of the sound pressure level (SPL), symbolized L_P:

$$L_P = 20\log_{10}(P / P_{ref}) \tag{3}$$

In this formula, P is the pressure amplitude and P_{ref} is the reference sound pressure. For underwater sound, the reference pressure is generally taken to be 1 µPa (10^{-6} Pa or 10^{-11} bar). In most cases, the sound intensity is directly proportional to the mean square of the sound pressure (i.e., $I \propto \langle P^2 \rangle$). Therefore, the sound pressure level (SPL) is usually taken to be synonymous with sound intensity level.

The decibel scale used for measuring hydroacoustic sound is not equivalent to the one used for measuring airborne sound. Airborne decibels are based on a standard reference pressure of 20 µPa, which is 20 times greater than the hydroacoustic reference pressure. Furthermore, due to differences in compressibility and density between the two media, the impedance relationship between sound pressure and sound intensity is not the same in air as it is in water. Taking into account differences in reference pressure and acoustic impedance, the hydroacoustic decibel

value (i.e., dB re 1 μPa in water) is approximately 63 dB greater than the standard airborne decibel value (i.e., dB re 20 μPa in air) for a sound wave with the same intensity in both media.

Since sound is a mechanical wave, it can also be measured in terms of the vibratory motion of fluid particles. Particle motion can be measured in terms of three different (but related) quantities: displacement, velocity, or acceleration. Acoustic particle velocity is the time derivative of particle displacement, and likewise acceleration is the time derivative of velocity. For the present study, acoustic particle motion has been reported in terms of velocity. Unlike sound pressure, particle motion is a vector quantity, meaning that is has both magnitude and direction: at any given point in space, acoustic particle motion has three different time-varying components (x, y, and z). Given the particle velocity in the x, y, and z, directions, v_x, v_y, and v_z, the particle velocity magnitude $|v|$ is computed according to the Pythagorean equation:

$$|v| = \sqrt{v_x + v_y + v_z} \tag{4}$$

The magnitude of the particle velocity can also be expressed in decibels, relative to a predefined reference level, v_{ref}:

$$L_v = 20 \log_{10}(|v| / v_{ref}) \tag{5}$$

For the current study, the standard reference velocity, v_{ref}, is taken to be 1 nm/s and particle velocity levels are quoted in units of dB re 1 nm/s.

Sounds that are composed of single frequencies are called “tones”. Most sounds are generally composed of a broad range of frequencies (“broadband” sound) rather than pure tones. Sounds with very short durations (less than a few seconds) are referred to as “impulsive”. Such sounds typically have a rapid onset and decay. Steady sounds that vary only slowly with time, or that do not vary at all, are referred to as “continuous”.

2.3.1. Continuous Noise

Continuous noise is characterized by gradual intensity variations over time. Propeller noise from a transiting ship is an example. The intensity of continuous noise is generally given in terms of the root-mean-square (*rms*) sound pressure. Given a measurement of the time varying sound pressure, $p(t)$, from a given noise source, the *rms* SPL (symbol L_P) is computed according to the following formula:

$$L_P = 10 \log_{10} \frac{1}{T} \int_T p(t)^2 dt / P_{ref}{}^2 \tag{6}$$

In this formula, T is the length of the time period over which the measurement was obtained. Figure 3 shows an example of a continuous noise pressure waveform and the corresponding *rms* sound pressure.

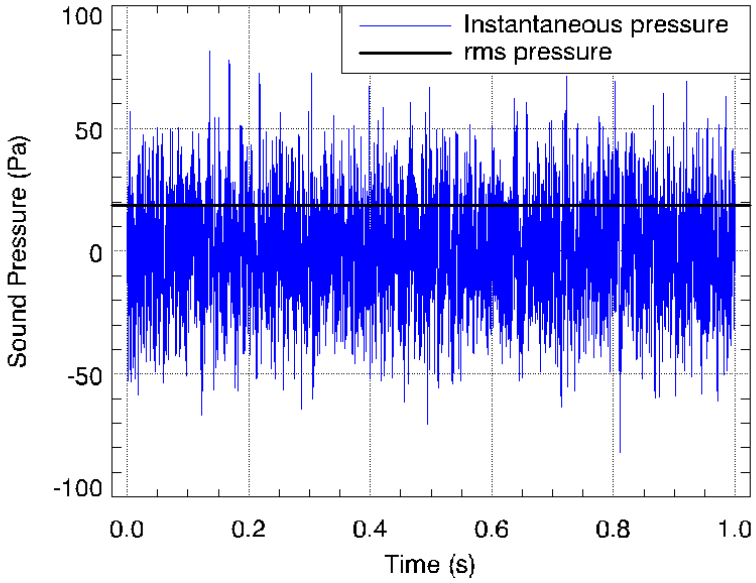

Figure 3. Example waveform showing a continuous noise measurement and the corresponding *rms* sound pressure.

2.3.2. Impulsive Noise

Impulsive or transient noise is characterized by brief, intermittent acoustic events with rapid onset and decay back to pre-existing levels (within a few seconds). Noise from impact driving of piles is an example. Impulse sound levels are commonly characterized using three different acoustic metrics: peak pressure, *rms* pressure, and sound exposure. The peak SPL (symbol L_{Pk}) is the maximum instantaneous sound pressure level measured over the impulse duration:

$$L_{Pk} = 20\log_{10}\left(\max\left|p(t)\right| / P_{ref}\right) \tag{7}$$

In this formula, $p(t)$ is the instantaneous sound pressure as a function of time, measured over the impulse duration $0 \le t \le T$. This metric is very commonly quoted for impulsive sounds but does not take into account the duration or bandwidth of the noise.

The *rms* sound pressure level may be measured over the impulse duration according to the following equation:

$$L_P = 10\log_{10}\left(\frac{1}{T}\int_T p(t)^2\,dt / P_{ref}^2\right) \tag{8}$$

Some ambiguity remains in how the duration T is defined, because in practice the beginning and end of an impulse can difficult to identify precisely. In studies of impulsive noise, T is often taken to be the interval over which the cumulative energy curve rises from 5% to 95% of the total energy. This interval contains 90% of the total energy (T_{90}), and the SPL computed over this interval is commonly referred to as the 90% *rms* SPL (L_{P90}). The relative energy, $E(t)$, of the impulse is computed from the time integral of the square pressure:

$$E(t) = \int_0^t p(\tau)^2\,d\tau / P_{ref}^2 \tag{9}$$

According to this definition, if the time corresponding to n% of the total relative energy of the impulse is denoted t_n, then the 90% energy window is defined such that $T_{90} = t_{95} - t_5$. Figure 4 shows an example of an impulsive noise pressure waveform, with the corresponding peak pressure, *rms* pressure, and 90% energy time interval.

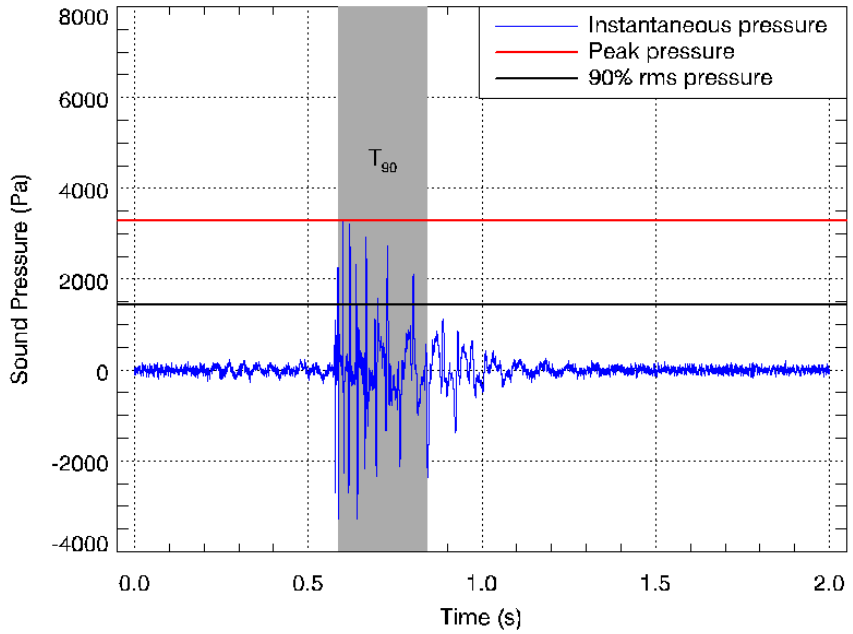

Figure 4. Example waveform showing an impulsive noise measurement. Horizontal lines indicate the peak pressure and 90% *rms* pressure for this impulse. The gray area indicates the 90% energy time interval (T_{90}) over which the *rms* pressure is computed.

The sound exposure level or SEL (symbol L_E) is a measure of the total sound energy contained in one or more impulses. The SEL for a single impulse is computed from the time-integral of the squared pressure over the impulse duration:

$$L_E = 10\log_{10}\left(\int_{T_{100}} p(t)^2\,dt / P_{ref}^2\right) = 10\log_{10}\left(E(t_{100})\right) \tag{10}$$

Unlike SPL, the SEL is generally applied as a dosage metric, meaning that its value increases with the number of exposure events. The cumulative SEL (cSEL) for multiple impulses (symbol $L_E^{(\Sigma)}$) is computed from the linear sum of the SEL values:

$$L_E^{(\Sigma)} = 10\log_{10}\left(\sum_{n=1}^{N} 10^{L_E^{(n)}/10}\right) \tag{11}$$

In this formula, N is the total number of impulses, and $L_E^{(n)}$ is the SEL of the n^{th} impulse event. Alternatively, given the mean (or expected) SEL for single impulse events, $\langle L_E \rangle$, the cumulative SEL from N impulses may be computed according the following formula:

$$L_E^{(\Sigma)} = \langle L_E \rangle + 10\log_{10}(N) \tag{12}$$

Sound exposure levels for impulsive noise sources (i.e., impact hammer pile driving) presented in this report refer to single pulse SELs as well as cumulative SELs (cSELs) where appropriate. Because the 90% *rms* SPL and SEL for a single impulse are both computed from the integral of square pressure, these metrics are related by a simple expression that depends only on the duration of the 90% energy time window T_{90}:

$$L_E = L_{P90} + 10\log_{10}(T_{90}) + 0.458 \quad (13)$$

In this formula, the 0.458 dB factor accounts for the remaining 10% of the impulse energy that is excluded from the 90% time window.

2.3.3. Source Level and Transmission Loss

Sources of underwater noise, such as ships' propellers or marine mammals' calls, generate radiating sound waves whose intensity generally decays with distance from the source. The dB reduction in sound level that results from propagation of sound away from an acoustic source is called propagation loss or transmission loss (TL). The loudness or intensity of a noise source is quantified in terms of the source level (SL), which is the sound level referenced to some fixed distance from a noise source. The standard reference distance for underwater sound is 1 m. By convention, transmission loss is quoted in units of dB re 1 m and underwater acoustic source levels are specified in units of dB re 1 µPa at 1 m. In the source-path-receiver model of sound propagation, the sound level L at some receiver position $\mathbf{r}$ is equal to the source level minus the transmission loss along the propagation path between the source and the receiver:

$$L(\mathbf{r}) = SL - TL(\mathbf{r}) \quad (14)$$

2.3.4. Spectral Density and 1/3-octave Band Analysis

The discussion of noise measurement presented so far has not addressed the issue of frequency dependence. The sound power per unit frequency of an acoustic signal is described by the power spectral density (PSD) function. The PSD for an acoustic signal is normally computed via the Discrete Fourier Transform (DFT) of time-sampled pressure data. The units of power spectral density are µPa^2/Hz or dB re 1 µPa^2/Hz. For practical quantitative spectral analysis a coarser representation of the sound power distribution is often better suited. In 1/3-octave band analysis, an acoustic signal is filtered into multiple, non-overlapping pass-bands before computing the SPL. 1/3-octave bands are defined so that three adjacent bands span approximately one octave (i.e., a doubling) of frequency. Figure 5 shows an example of power spectral density levels and corresponding 1/3-octave band pressure levels for an ambient noise recording.

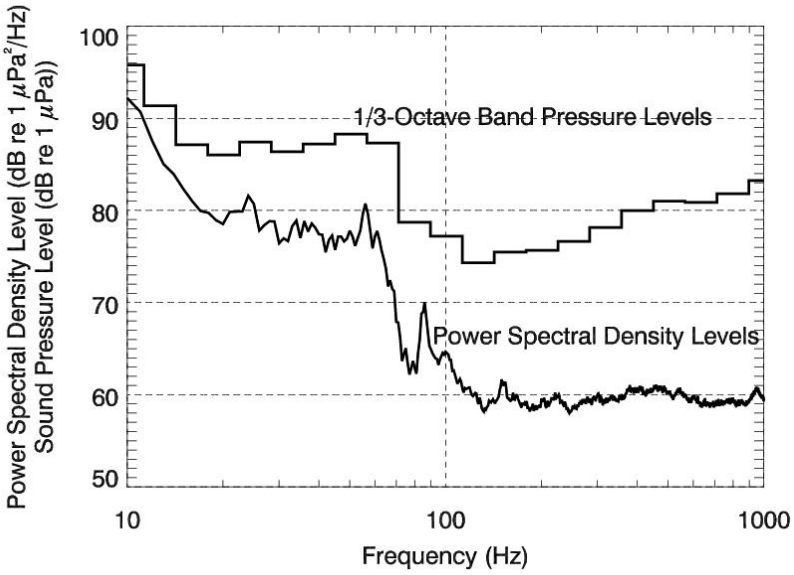

Figure 5. Plot of an ambient noise power spectrum and corresponding 1/3-octave band levels. Frequency is plotted on a log scale so 1/3-octave bands are wider at higher frequencies.

Standard center frequencies for 1/3-octave pass bands are given by the following formula:

$$f_c(n) = 10^{n/10} \quad n = 1, 2, 3... \tag{15}$$

Nominal 1/3-octave band center frequencies, according to ISO standards, for the range relevant to this study are listed in Table 1. The SPL inside a 1/3-octave band, $L_{pb}(f_c)$, is related to the average PSD level inside that frequency band, $L_{ps}^{(avg)}(f_c)$, by the bandwidth, Δf:

$$L_{ps}^{(avg)}(f_c) = L_{pb}(f_c) - 10\log_{10}(\Delta f) \tag{16}$$

The bandwidth of a 1/3-octave band is equal to 23.1% of the band center frequency (i.e., $\Delta f = 0.231 f_c$). Spectrum density levels and band levels are not limited to measurements of sound pressure: they may also, with appropriate selection of reference units, be given for SEL and particle velocity measurements.

Table 1: Nominal 1/3-octave band center frequencies from 10 Hz to 8 kHz.

Band Number	*Center Frequency (Hz)*	*Band Number*	*Center Frequency (Hz)*	*Band Number*	*Center Frequency (Hz)*
10	10	20	100	30	1000
11	12.5	21	125	31	1250
12	16	22	160	32	1600
13	20	23	200	33	2000
14	25	24	250	34	2500
15	31.5	25	315	35	3150
16	40	26	400	36	4000
17	50	27	500	37	5000
18	63	28	630	38	6300
19	80	29	800	39	8000

2.4. Effects Thresholds

The potential impact of anthropogenic (man-made) noise on a marine animal depends on the level of noise exposure. At moderate exposure levels, underwater noise may cause an overt change in the behavior of a subject. At high exposure levels, underwater noise can induce a temporary or permanent reduction in hearing sensitivity. At extreme exposure levels, pressure waves from some noise sources can cause traumatic injury and death. The impact of noise exposure generally depends on a number of factors related to the physical properties of the sound (e.g., the intensity, peak pressure, frequency, duration, duty cycle), and to the animal under consideration (e.g., hearing sensitivity, age, gender, behavioral status, prior exposures). The manner and severity of the impact can also depend on whether the overall noise consists of impulsive or continuous sounds or a combination. Common behavioral responses to noise exposure include startle or avoidance. Physiological effects usually consist of a lessening of the subject's hearing sensitivity. This reduction can be characterized as a temporary threshold shift (TTS) or permanent threshold shift (PTS), depending on whether hearing sensitivity recovers after the exposure. At extreme intensity levels, exposure to certain kinds of noise can cause physical trauma or death. Effect threshold criteria (sound levels deemed to induce onset of certain effects in a given species or category of animals) are generally used to establish zones of impact around marine noise sources for assessment or mitigation purposes.

Of the various construction activities associated with the Project, impact hammer pile driving is expected to generate the highest underwater sound levels. Based on a review of the available scientific data, an interim set of effects thresholds for fishes exposed to pile driving noise has been proposed for the Project's EIS. The proposed criteria for onset of physiological effects are as follows:

Peak SPL	208 dB re 1 µPa
Single strike SEL	187 dB re 1 $\mu Pa^2 \cdot s$
cSEL	197 dB re 1 $\mu Pa^2 \cdot s$

These criteria address physiological effects only, and are considered conservative for Hudson River fish species based on the available literature.

3. Methods

3.1. Sound Propagation Models

3.1.1. Marine Operations Noise Model

Acoustic footprints for marine construction activities in Tappan Zee Reach were modeled using JASCO Applied Sciences' proprietary Marine Operations Noise Model (MONM). MONM generates accurate estimates of the ensonfication of an underwater environment surrounding construction activities using a sophisticated numerical acoustic propagation algorithm. This algorithm fully accounts for the spectral distribution of the source and the physics of sound propagation in the water column and the underlying geological substrates. This type of modeling

differs significantly from generalized and empirical acoustic models, such as “practical spreading loss” models (see CALTRANS 2009, 4-16) that do not take into full account the source characteristics or the many site-specific factors that influence the rate of noise attenuation.

The propagation modeling algorithm in MONM is based on the U.S. Naval Research Laboratory’s split-step Padé parabolic equation (PE) range-dependent acoustic model (RAM). RAM has been extensively benchmarked for accuracy and is widely employed in the underwater acoustics community (Collins, 1993). The split-step Padé solution is not only valid for very wide vertical propagation angles (> 60 degrees in most cases) but it also fully accounts for the geoacoustic properties of the sub-bottom and the discontinuity of these properties at the interface (Jensen et al., 2000, Ch. 6). Furthermore, JASCO has augmented RAM to account for losses due to the elastic (that is, shear-wave) properties of the sub-bottom using the complex density equivalent fluid approximation (Zhang and Tindle, 1995). The combination of the wide-angled PE and the accurate handling of the sub-bottom geoacoustic properties mean that JASCO's approach is completely applicable in shallow water environments.

MONM computes acoustic fields in 3-D by modeling transmission loss along evenly distributed radial traverses covering a 360 º swath from the source (so-called N×2-D modeling). The model makes use of several parameters of the propagation environment including bathymetry, sound speed profiles in water and geoacoustic profiles. Underwater sound propagation is strongly influenced by the geoacoustic properties of the riverbed, which include the material density, seismic compressional-wave (P-wave) and shear-wave (S-wave) speeds, and the seismic wave-attenuation of seabed materials. MONM takes each of these into account when calculating propagation loss. Frequency dependence of the sound propagation is treated by computing acoustic transmission loss in 1/3-octave bands up to several kHz. Sound pressure levels in each band are computed by applying frequency-dependent transmission losses to the corresponding 1/3-octave band source levels. Broadband results are then obtained by summing the levels across all bands. Results from multiple model runs for concurrently operating sources may be meshed into multi-source scenario results. This approach has been validated against benchmarks and experimental data and has proven to be highly accurate for predicting noise levels in the vicinity of industrial operations associated with marine construction and geophysical survey activities (Hannay and Racca, 2005).

The parabolic-equation (PE) based algorithm at the core of MONM, represents the best available method for modeling underwater sound propagation in complex-bathymetry environments like Tappan Zee Reach. While the PE algorithm assumes that sound originates from a single source in the water column (i.e., the "far-field" approximation) rather than a distributed source along the struck pile, the method of effective source level estimation by back-propagation (to be discussed in Section 3.2) ensures that modeled acoustic levels are calibrated against actual pile driving measurements. Back-propagated source levels necessarily account for sound energy from all different propagation paths that contributed to the original measurement, originating both in the water column and below the mudline. Averaging over an ensemble of measurements further ensures the generality of the derived source levels. MONM applies the propagation loss, based on the dominant water-borne path, to the back-propagated source levels to determine the attenuation of sound energy with distance from the pile. Sound levels computed by this method, which is commonly used in the field of hydroacoustics, are expected to be conservative in the near-field and accurate in the far-field.

3.1.2. VSTACK Near-field Wavenumber Integration Model

Near-field peak pressure and particle velocity from marine pile driving were modeled using JASCO's VSTACK wavenumber integration model. VSTACK computes synthetic pressure waveforms versus depth and range for arbitrarily layered acoustic environments using the wavenumber integration approach to solving the exact (range-independent) acoustic wave equation. This model is valid over the full angular range of the wave equation and can fully account for the elasto-acoustic properties of the sub-bottom. Wavenumber integration methods are extensively used in the field of underwater acoustics and seismology where they are often referred to as reflectivity methods or discrete wavenumber methods (Jensen et al., 2000). VSTACK computes sound propagation in arbitrarily stratified water and seabed layers by decomposing the outgoing field into a continuum of outward-propagating plane cylindrical waves. Seabed reflectivity in VSTACK is dependent on the seabed layer properties: compressional and shear wave speeds, attenuation coefficients, and layer densities. VSTACK fully accounts for vibration of the seabed interface excited by the pile and its coupling to the water column. Fundamental to the modeling is the physical constraint that the instantaneous displacements of the seabed and the water are equivalent at the interface between the two media.

VSTACK computes pressure waveforms via Fourier synthesis of the acoustic transfer function in closely spaced (< 1 Hz) frequency bands. In addition, VSTACK includes the ability to model distributed monopole sound sources in the water column and in the sub-bottom. A vertically-distributed array of sources is used to calculate both pressure and particle velocity in the near-field region of a pile. VSTACK assumes range-invariant bathymetry with a horizontally stratified medium (i.e., a range-independent environment) which is azimuthally symmetric about the source. VSTACK is thus best suited to modelling the sound field in close proximity to the pile. Note that, while the range-independent model assumes that the layering of the environment is invariant with range, it does not assume that the vibration field is invariant with range. Even in the range-independent case, the vibration field exhibits very complex variations with distance from the source. This is due to interference between the multiple acoustic paths corresponding to reflection and transmission of vibration from the different layers in the model, which VSTACK accounts for in its calculation.

3.1.3. FWRAM Far-field Waveform Synthesis Model

For computing *rms* SPLs from marine pile driving, far-field pressure waveforms were modeled along single-range depth transects using JASCO's FWRAM time-domain PE model. FWRAM computes synthetic pressure waveforms versus range and depth for range-varying marine acoustic environments using the parabolic equation approach to solving the acoustic wave equation. This software uses the same underlying algorithmic engine as MONM for computing acoustic propagation along 2-D range-depth transects, and takes the same environmental inputs (bathymetry, water sound speed profiles, and seabed geoacoustics). FWRAM computes pressure waveforms via Fourier synthesis of the modelled acoustic transfer function in closely spaced frequency bands. Like MONM, FWRAM accounts for range-varying properties of the acoustic environment and is therefore capable of computing *rms* SPL at long ranges, outside the near-field zone of the pile driving. FWRAM, being a time-domain model, is well suited to computing time-averaged *rms* SPL values for impulsive sources.

3.2. Acoustic Source Levels

Source levels for impact hammer pile driving scenarios were estimated based on a review and analysis of published sound level measurements from the available literature. Documentation provided by the Project's engineers specified that 4 ft, 6 ft, 8 ft, and 10 ft diameter steel piles would be driven at the proposed bridge site using two different types of hydraulic impact hammers: IHC model S-750 rated to 550.8 kips-ft and IHC model S-600 rated to 443.5 kips-ft. Direct measurements of underwater sound levels for these specific hammer-pile combinations were unavailable; source levels were therefore estimated from analysis of published pile driving measurements (Table 2). These studies presented received levels in spectra or 1/3-octave bands for a variety of pile-hammer configurations, measured in different acoustic environments. Table 2 specifies the pile size, hammer energy, measurement range, measured broadband SEL and frequency range for the measurements that were used to derive acoustic source levels. Source levels for the current study were extrapolated from these data based on hammer energy and pile dimensions, which are the primary factors that determine sound emissions from impact pile driving (Nehls et al, 2007, §2.1.3).

Table 2: Specifications of pile driving measurements from published literature.

Project	Pile Diameter (ft)	Hammer Type	Rated Hammer Energy (kips·ft)	Measurement Range (ft)	SEL at Measurement Range (dB re 1 $\mu Pa^2 \cdot s$)	Reported Frequency Range (Hz)
Eagle Harbor 2005 [a]	3.0	Diesel	138	33	179	10-16000
NaiKun 2007 [b]	3.0	Drop	236	33	192	10-16000
Alameda 2006 [c]	3.3	Diesel	221	33	180	10-5000
ITAP 2006 [d]	7.2	Hydraulic	145	98	174	12.5-20000
PIDP 2001 [e]	7.9	Hydraulic	738	328	178	50-20000
Richmond 2003 [f]	5.5	Diesel	266	98	173	10-5000
Amrumbank 2005 [g]	11.5	Unknown	406	2789	174	30-20000
FINO2 2006 [g]	10.8	Hydraulic	221	1739	173	16-20000
Utgrunden 2000 [h]	9.8	Hydraulic	299*	1050	173	16-12000

Citations: (a) MacGillivray et al. 2005, (b) Racca et al., 2007, (c) Illingworth and Rodkin Inc., 2006, (d) Schultz et al., 2006, (e) Caltrans, 2001, (f) Reyff, 2003, (g) Nehls et al., 2007, (h), McKenzie-Maxon, 2000.
*The hammer energy was not specified for the Utgrunden project. The energy estimate used for the source level calculations, 299 kips-ft, was set lower than both hammer energies proposed in an attempt to derive conservative source levels.

To calculate 1/3-octave band source levels, the measured spectra were first converted to 1/3-octave band received levels by summing the energy in each band. Each measurement was back-propagated to 1 m (3.28 ft) from the source assuming spherical spreading – i.e. by adding $20\log_{10}r$ to the received levels, where r is the measured distance to the pile in meters. At closer distances to the pile, where source levels measurements are preferentially obtained, spherical spreading is expected to accurately represent the mean propagation loss. This is particularly the case when averaging over several different measurements, as has been done here. Spherical spreading may underestimate source levels at some lower frequencies, where bottom loss has greater influence; however, these frequencies are rapidly attenuated with range and do not make a dominant contribution to the far-field sound levels.

The resulting 1/3-octave band source levels were then scaled to a common reference hammer energy assuming that the underwater acoustic energy was directly proportional to the hammer energy – i.e. by adding $10\log_{10}(E_{ref}/E_{ham})$ to the source levels, where E_{ref} is a reference energy

and E_{ham} is the maximum rated energy of the hammer used during the particular measurement. The energy-corrected broadband source level for each measurement was plotted against pile diameter, and linear regression was used to derive the trend of the data (see Figure 6).

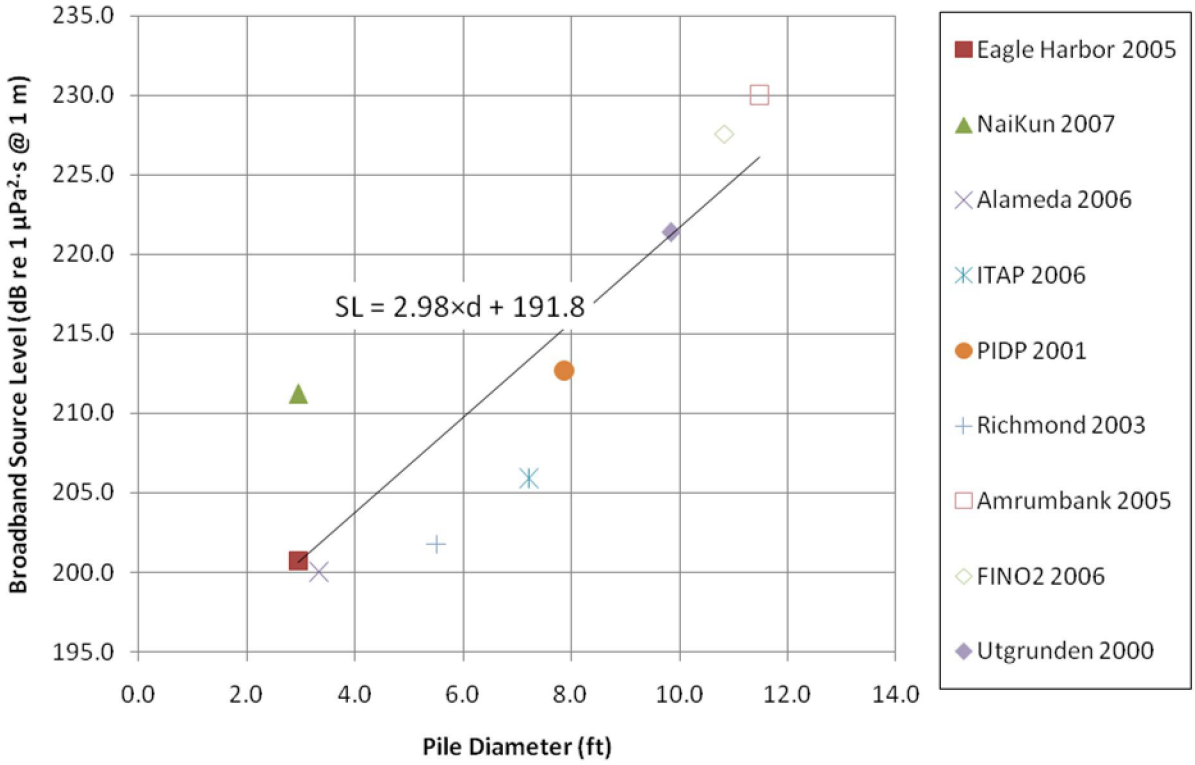

Figure 6. Energy-corrected broadband source level for pile driving as a function of pile diameter. The equation of the regression fit is annotated on the plot, where *d* is in ft and *SL* is in dB re 1 µPa^2·s @ 1 m. Refer to Table 2 for citations.

The resulting energy-corrected 1/3-octave band source levels showed two trends that were dependent on pile size. Levels for small diameter piles (4-6 ft) were highest at frequencies between approximately 200 and 1260 Hz; levels for large diameter piles (8-10 ft) were highest at frequencies between approximately 100 and 630 Hz. Source levels in each 1/3-octave band were averaged for all measurements, in their pile size range, to characterize the frequency distribution for small and large piles. Figure 7 shows the resulting averaged 1/3-octave band source levels for small and large piles.

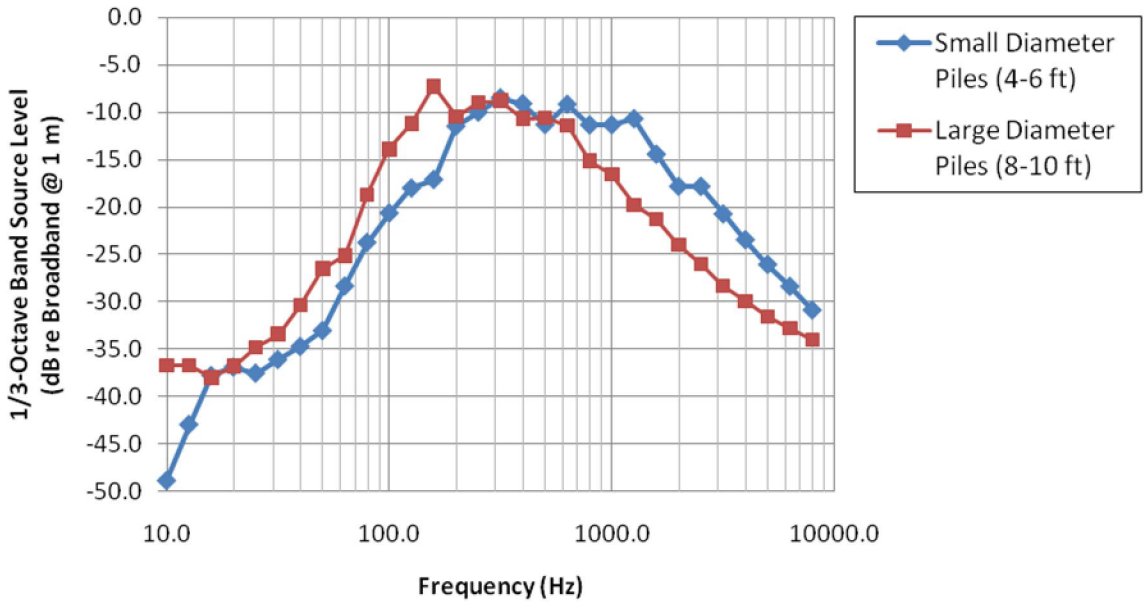

ZZ

Figure 7. Normalized 1/3-octave band source levels, corrected for hammer energy, for small (4-6 ft) and large (8-10 ft) diameter piles.

To calculate the 1/3-octave band source levels for each proposed pile-hammer configuration, the appropriate frequency distribution (small or large diameter) was adjusted so that the broadband level matched the level predicted by the regression equation in Figure 6 for the pile size in question. The source levels were then adjusted from the reference hammer energy to the rated hammer energy for the proposed hammer by adding $10\log_{10}(E_{ham}/E_{ref})$ to the estimates. Figure 8 shows the 1/3-octave band source levels for the four pile-hammer configurations used in this modeling study.

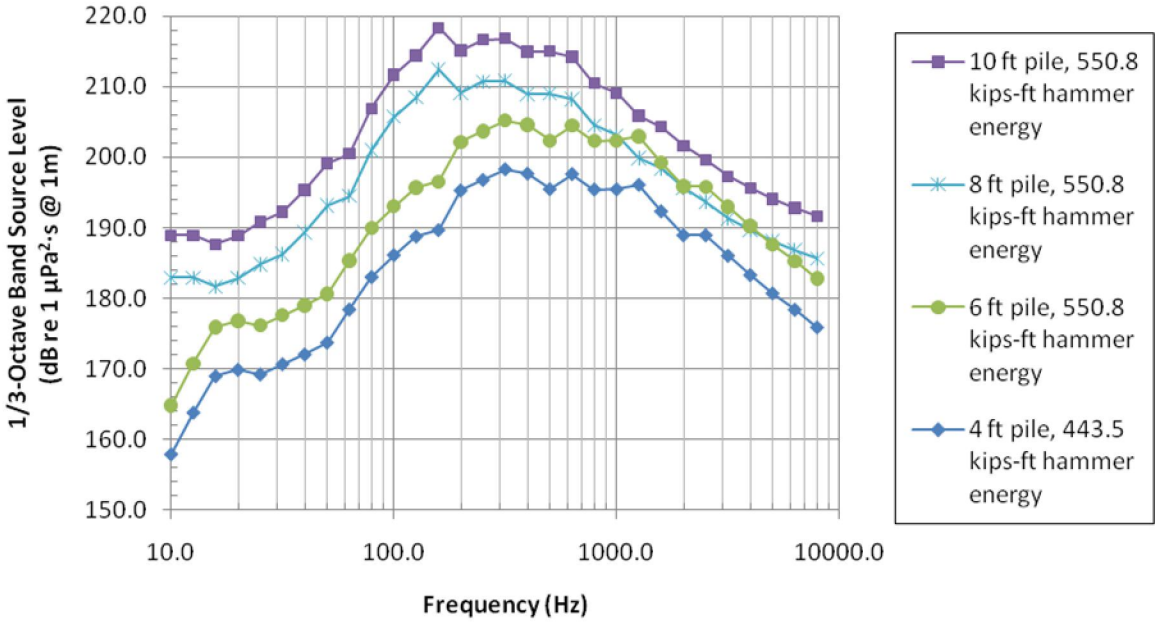

Figure 8. Estimated 1/3-octave band source levels for impact driven steel piles with specified diameter and pile energy.

Estimates of peak SPLs and *rms* SPLs require time-domain representations of source impulses generated in the water by the impact hammer pile driving. Direct-path measurements of source waveforms from pile driving are generally difficult to extract from recorded data because pile driving tends to take place in shallow water where, even at very close range, direct-path source waveforms are contaminated by interference from multiple bottom and surface reflections. For the current study, source wavelets for the piling were instead derived mathematically from the 1/3-octave band source levels via spectral factorization (Claerbout, 1976). The spectral factorization algorithm derives a unique time-domain waveform from a given power spectrum by compressing the maximum amount of signal energy into the shortest causal time period (known as the minimum-phase condition). Far-field source waveforms derived via spectral factorization (Figure 9) are expect to provide a realistic but conservative estimate of peak pressures generated during impact hammer pile driving.

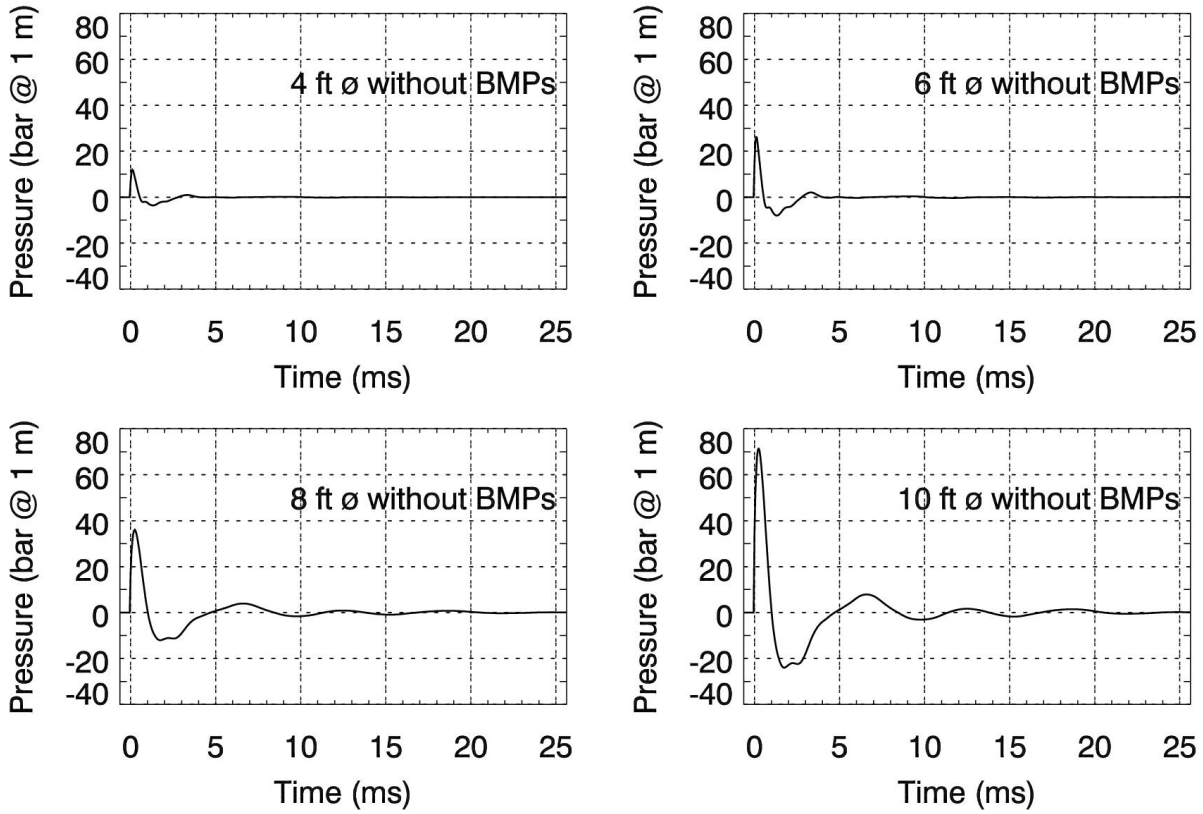

Figure 9. Far-field source waveforms for impact pile driving, referenced to 1 m range, as derived from spectral factorization of 1/3-octave band source levels.

3.3. Best Management Practices (BMPs)

Best Management Practices (BMPs) consist of strategies that may be applied to reduce impacts of construction activities on the surrounding environment. For aquatic pile driving, BMPs are focused primarily on methods for reducing sound levels of waterborne pressure waves. Examples of BMPs for aquatic pile driving include the following:

1. Air bubble curtains (confined and unconfined)
2. Pile sleeves and other physical barriers
3. Working in dewatered cofferdams
4. Vibratory driving instead of impact driving
5. Pile driving cushions

For locations with notable current velocity, like the Tappan Zee Reach, experience has shown that confined air bubble curtains, which consist of one or more bubble rings enclosed in a sleeve surrounding the pile, represent a practical BMP strategy. The application of air bubble curtains for reducing underwater sound levels from pile driving has been studied extensively, particularly for large diameter piles (Vagle, 2003, Nehls et al., 2007, CALTRANS, 2009). The operating principle of this mitigation method is based on the fact that a cloud of air bubbles generated

around the pile changes the acoustic properties of the medium in such a way as to reduce transmission of pressure waves from pile driving into the surrounding water. The reported effectiveness of bubble curtains is highly variable and depends on many factors, including the thickness of the bubble layer, the total volume of injected air, the size of the bubbles relative to the sound wavelength, and whether the curtain is completely closed. Use of a confined air bubble curtain ensures that the submerged section of a pile is shielded from water currents and remains completely enshrouded in bubbles at all times. On the basis of these considerations, confined air bubble curtains were identified as the best probable BMP strategy for the Project.

A review of the available literature yielded a number of measurements of sound attenuation for confined air bubble curtain systems. Of the available data, the relatively few measurements that showed per-frequency comparisons of attenuated and non-attenuated impact piling sound levels were compiled to determine an average attenuation trend for confined air bubble curtain systems (Table 3 and Figure 10). Averaging of 1/3-octave band attenuation levels was limited to the frequency range for which all literature sources reported data (63 Hz to 6300 Hz). While the mean broadband attenuation was found to be approximately 20 dB, the published measurements showed substantial variability in the effectiveness of confined air bubble curtain systems with quoted broadband sound level reductions ranging from 5 dB to 36 dB.

Based on published assessment guidelines (CALTRANS, 2009, 2-25, and WSDOT, 2010b, 7.41) it was determined on precautionary grounds that 10 dB mean attenuation was a more realistically achievable target for BMP performance. The average attenuation trend from the literature review analysis was therefore adjusted downwards for the modeling so that the mean 1/3-octave band attenuation in the range 63 Hz to 6300 Hz was equal to 10 dB (Figure 11). This adjustment resulted in extrapolated attenuation values of approximately 0 dB (no mitigation effect) below 63 Hz, which is consistent with the typically poor low-frequency performance of bubble curtain systems apparent in Figure 10. The confined air bubble curtain attenuation values thus derived were applied to source levels for those modeling scenarios that included BMPs. The same BMP attenuation values were also applied, as appropriate, to the time-domain source waveforms for peak SPL and *rms* SPL modeling scenarios.

Table 3: Specifications of confined air bubble curtain systems from published literature sources for impact driving of steel shell piles.

Project	BMP Description	Air Curtain Specifications*	Pile Diameter (ft)	Meas. Distance (ft)	Quoted Reduction (broadband)
WSDOT SR-520 [(a)]	Steel isolation casing with single bubble ring	680-700 CFM 105-115 PSI	2.5	33	35 dB
Benicia-Martinez Bridge [(b)]	Steel isolation casing 12.1 ft diameter with bubble ring	unkown	7.9	177	21 dB
East Span PIDP [(c)]	Fabric mantle 13.1 ft diameter with bubble ring	1500 CFM	8.5	330	5-10 dB
WSF Eagle Harbor [(d)]	PVC isolation casing 4 ft diameter with single bubble ring	300-350 CFM	2.0	33	9 dB

Citations: (a) WSDOT, 2010a, (b) CALTRANS, 2009, (c) Illingworth and Rodkin, 2001, (d) MacGillivray and Racca, 2005.

* CFM = cubic feet per minute (airflow rate), PSI = pounds per square inch (air pressure).

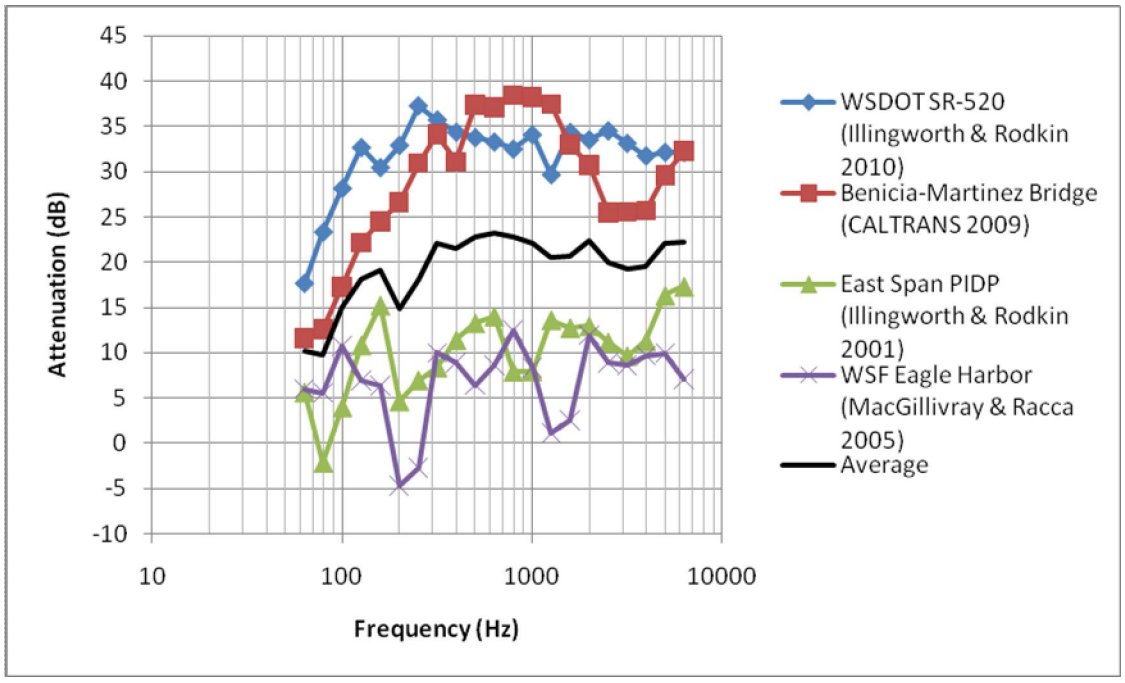

Figure 10. Published measurements of acoustic attenuation for confined air bubble curtain systems in 1/3-octave bands. Black line indicates average attenuation in each frequency band.

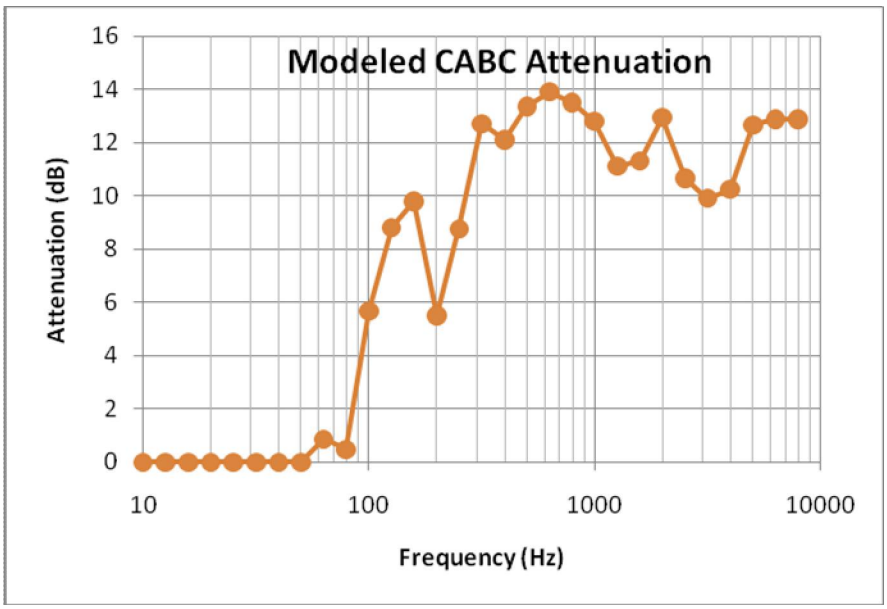

Figure 11: Modeled acoustic attenuation for a confined air bubble curtain system in 1/3-octave frequency bands.

3.4. Acoustic Environment

3.4.1. Bathymetry

JASCO's acoustic models utilize high-resolution grids of bathymetry data to define water depths inside a region of interest. For the current study, high-resolution bathymetric survey data from Ocean Surveys, Inc. (OSI) were combined by AECOM with bathymetric data from publicly available sources (such as NYSDEC and NOAA) to produce the gridded bathymetric dataset used in the acoustic propagation model. The spatial resolution of the gridded dataset was 67 ft (20 m). Water depths were corrected to Mean Sea Level (MSL) (0.08 ft above NAVD88) before being input to the model. The gridded bathymetry dataset (Figure 12) extended approximately 65,000 ft upriver and 65,000 ft downriver from the location of the proposed bridge crossing.

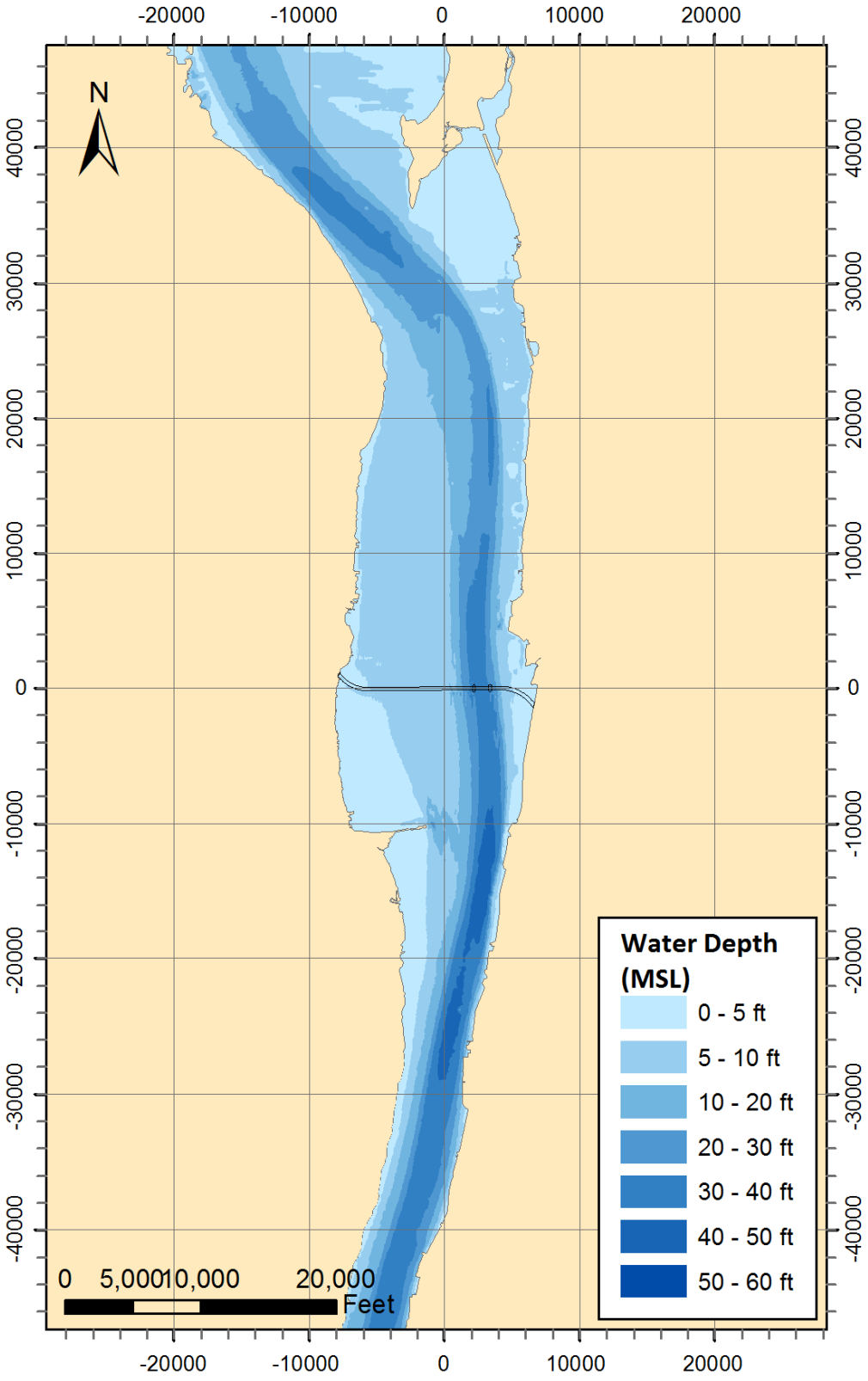

Figure 12: Contour map of Hudson River bathymetry data used in the acoustic modeling. Map grid shows coordinates, in feet, relative to the bridge center.

3.4.2. Underwater sound speed

Temperature and salinity are the most important factors that determine the speed of sound in water. For the current study, river sound speed profiles were derived from conductivity-temperature-depth (CTD) survey data collected at Tappan Zee Reach by OSI in April 2007, October 2008, and December 2008 (OSI, 2009). Profiles from the CTD survey showed that temperature was fairly uniform with depth for all survey periods (typically < 2°F variation), with April temperatures colder at the bottom and December temperatures colder at the surface. Salinity stratification was more variable than temperature stratification: both the April and December profiles showed a strong halocline (~8 PSU), whereas the October data did not.

The weak stratification of the October profiles corresponded to a nearly uniform distribution of sound speed with depth. Given the observed temporal variability, a uniform sound velocity profile was considered to best reflect the mean conditions in Tappan Zee Reach; the October conditions were thus selected as representative for the modeling. Seven CTD records collected on 31 October 2008 within 2500 ft of the existing Tappan Zee Bridge were combined to derive a uniform underwater sound speed profile representative of conditions near the bridge (Figure 13), which was used as input to the acoustic models. The sound speed profiles shown were computed directly from temperature and salinity values using standard formulae (Coppens, 1981).

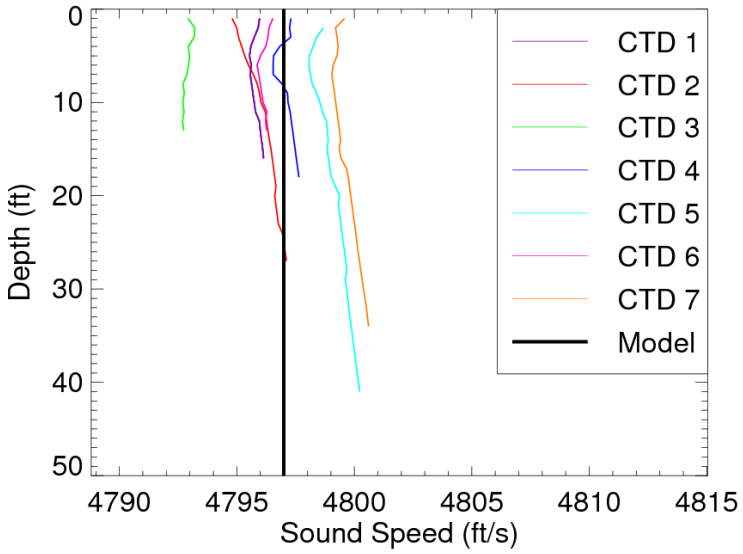

Figure 13: Model sound speed profile as derived from temperature and salinity measurements obtained during October 2008 in Tappan Zee Reach.

3.4.3. Riverbed geoacoustics

Geoacoustic profiles, describing the elasto-acoustic properties of the riverbed sediments, were estimated from geological stratigraphy data for the bridge span documented by NYSDOT (Arup, 2010, Lacey, 2008). A cross-section of the riverbed stratigraphy at the Tappan Zee Bridge site showed that it is composed primarily of five layered units: organic silty clay, organic silty clay with sand, sand, glacial varved silt and clay, and bedrock. The thicknesses and depths of these

layers vary across the span of the river. Descriptions of soil composition for these layers were used to estimate geoacoustic properties using the methods described by Hamilton (1980).

In order to account for variations in the layering of the riverbed sediments, unique site-specific geoacoustic profiles were created for each of the source locations used in the modeling (Table 4); these profiles were used for modeling sound propagation at ranges up to 820 ft from the piles. At longer distances from the piles, the range-dependent models (MONM, FWRAM) transitioned to a common geoacoustic profile, also shown in Table 4, intended to represent mean sediment properties over the span of the river. Riverbed properties near the pile are more influential than those at long ranges, since bottom loss at the source determines the total amount of sound energy that remains trapped in the water column. Geoacoustic properties were defined up to a maximum depth of 340 ft below the riverbed, which was the maximum depth of the available geological data.

The five geoacoustic properties used by MONM for modeling sound propagation in sub-bottom sediments are as follows:

1. Relative density: The density of the bottom materials relative to the density of water.
2. Compressional-wave sound speed: The phase speed of longitudinal body waves (P-waves) in the bottom materials (units of ft/s).
3. Compressional attenation: The rate of attenuation (units of dB per wavelength) of longitudinal body waves in the bottom materials.
4. Shear-wave sound speed: The phase speed of transverse body waves (S-waves) in the bottom materials (units of ft/s).
5. Shear attenuation: The rate of attenuation (units of dB per wavelength) of transverse body waves in the bottom materials.

In MONM, profiles of density, compressional-wave speed, and compressional attenuation may be defined to arbitrary depth in the sub-bottom. The complex-density fluid approximation used by MONM accounts for bottom loss due to shear-wave conversion at the seabed interface. In this approximation, shear-wave properties of the sediments are only modelled at the water-riverbed interface. Shear-wave properties of the deeper layers do not significantly influence sound propagation in the water column and are not incorporated into the complex-density approximation.

Table 4. Site-specific geoacoustic profiles for each of the seven pile modeling locations (identified by dual/single construction pier number). The last profile in the table is the average river geoacoustic profile that was common to all model scenarios at distances > 820 ft from the source.

Depth (ft below riverbed)	Soil Description	Relative Density (water=1)	Compressional Sound Speed (ft/s)	Compressional Attenuation (dB/λ)	Shear Sound Speed (ft/s)	Shear Attenuation (dB/λ)
P8/P15						
0	Organic silty clay	1.42	4768	0.11	361	1.9
80		1.45	4848	0.12	–	–
80	Organic silty clay with sand	1.63	5035	0.32	–	–
160		1.65	5115	0.46	–	–
160	Sand	2.00	5796	0.87	–	–
175		2.01	5812	0.87	–	–
175	Glacial varved silt and clay	1.55	5039	0.17	–	–
340		1.61	5204	0.27	–	–
P12/P23						
0	Organic silty clay	1.42	4768	0.11	361	1.9
80		1.45	4848	0.12	–	–
80	Organic silty clay with sand	1.63	5035	0.32	–	–
115		1.64	5070	0.38	–	–
115	Sand	2.00	5751	0.86	–	–
175		2.02	5812	0.86	–	–
175	Glacial varved silt and clay	1.55	5039	0.17	–	–
340		1.61	5204	0.27	–	–
P16/30						
0	Organic silty clay	1.42	4768	0.11	361	1.9
100		1.46	4868	0.13	–	–
100	Organic silty clay with sand	1.63	5055	0.36	–	–
140		1.65	5095	0.43	–	–
140	Sand	2.00	5776	0.87	–	–
165		2.01	5801	0.87	–	–
165	Glacial varved silt and clay	1.55	5029	0.16	–	–
340		1.61	5204	0.27	–	–
P20/38						
0	Organic silty clay	1.42	4768	0.11	361	1.9
85		1.45	4853	0.12	–	–
85	Organic silty clay with sand	1.63	5040	0.33	–	–
105		1.63	5060	0.36	–	–
105	Sand	2.00	5741	0.86	–	–
135		2.01	5771	0.86	–	–
135	Glacial varved silt and clay	1.54	4999	0.16	–	–
190		1.56	5054	0.17	–	–
190	Rock	2.20	7216	0.10	–	–

Depth (ft below riverbed)	Soil Description	Relative Density (water=1)	Compressional Sound Speed (ft/s)	Compressional Attenuation (dB/λ)	Shear Sound Speed (ft/s)	Shear Attenuation (dB/λ)
P24/44						
0	Organic silty clay	1.42	4768	0.11	361	1.9
70		1.45	4838	0.12	–	–
70	Organic silty clay with sand	1.62	5025	0.31	–	–
75		1.62	5030	0.32	–	–
75	Sand	2.00	5711	0.86	–	–
95		2.01	5731	0.86	–	–
95	Glacial varved silt and clay	1.52	4959	0.15	–	–
230		1.57	5094	0.18	–	–
230	Rock	2.20	7216	0.10	–	–
P25/45						
0	Organic silty clay	1.42	4768	0.11	361	1.9
75		1.45	4843	0.12	–	–
75	Organic silty clay with sand	1.62	5030	0.32	–	–
85		1.63	5040	0.33	–	–
85	Sand	2.00	5721	0.86	–	–
100		2.01	5736	0.86	–	–
100	Glacial varved silt and clay	1.52	4964	0.15	–	–
230		1.57	5094	0.18	–	–
230	Rock	2.20	7216	0.10	–	–
P27/48						
0	Organic silty clay	1.42	4768	0.11	361	1.9
25		1.43	4793	0.12	–	–
25	Organic silty clay with sand	1.61	4980	0.23	–	–
80		1.63	5035	0.32	–	–
80	Sand	2.00	5716	0.86	–	–
100		2.01	5736	0.86	–	–
100	Glacial varved silt and clay	1.52	4964	0.15	–	–
145		1.54	5009	0.16	–	–
145	Rock	2.20	7216	0.1	–	–
Average						
0	Organic silty clay	1.42	4768	0.11	361	1.9
80		1.45	4848	0.12	–	–
80	Organic silty clay with sand	1.63	5035	0.32	–	–
110		1.64	5065	0.37	–	–
110	Sand	2.00	5747	0.86	–	–
140		2.01	5776	0.86	–	–
140	Glacial varved silt and clay	1.54	5004	0.16	–	–
400		1.63	5264	0.38	–	–
400	Rock	2.20	7216	0.10	–	–

3.5. SEL and cSEL Modeling

MONM was used to directly compute single-strike SEL and cumulative SEL produced by marine pile driving activities at Tappan Zee Reach. Acoustic fields were computed on a three-dimensional spatial grid, resolved into 1/3-octave frequency bands. For subsequent presentation and interpretation, sound levels from MONM were rendered as two-dimensional contour maps that showed the acoustic footprint maximized over the depth dimension. Two different kinds of impact pile driving scenarios were modeled for the current study: single-pile, single-strike SEL scenarios, and multi-pile, multi-strike cSEL scenarios. The single-pile, single-strike scenarios considered the SEL field produced by a single hammer blow at a single location. The multi-pile, multi-strike scenarios considered the total cSEL field produced by driving of multiple piles at several different locations over the course of a 12-hour work day.

The modeling procedure for the single-pile, single-strike SEL scenarios was as follows:

1. MONM was used to compute three-dimensional fields (range, azimuth, depth) of transmission loss for each pile driving source location in 1/3-octave frequency bands.
2. Single-strike SEL fields, in 1/3-octave bands, were computed by combining pile driving source levels (Section 3.2) with transmission loss.
3. The 1/3-octave band SEL fields for each pile were resampled onto a 10 m cartesian grid (easting, northing). A 100 m radial-smoothing kernel was applied to the SEL fields prior to gridding.
4. The 1/3-octave band SEL grids were summed over frequency and maximized over depth to generate a two-dimensional plane of received levels.
5. A contouring algorithm was used to extract SEL contours from the received level data.
6. SEL contours were converted to GIS layers and rendered on thematic maps.

The modeling procedure for the multi-pile, multi-strike cSEL scenarios was as follows:

1. Aligned grids of single-strike SEL values were computed for the individual source locations, according to steps 1-3 above.
2. For each individual source location, multi-strike cSEL was computed from the single-strike SEL according to the total number of pile driving hammer blows (i.e., by adding $10\log_{10}(N)$).
3. The cSEL results from all sources were summed at the aligned grid points to compute the multi-source cSEL.
4. The cSEL grids were converted to maximum-over-depth cSEL contours according to steps 4-6 above.

Acoustic propagation estimates generated by MONM are suitable for computing SEL and cSEL from aquatic pile driving operations in the acoustic far-field of the pile. The far-field region is where the distributed nature of the pile can be safely neglected for the purpose of computing propagation loss, treating the sound as radiating from a single point. The choice of this point is nonetheless important for generating propagation loss estimates. For modeling aquatic pile driving with MONM, the point of radiation was placed midway between the surface and the mudline as this provides the maximum acoustic excitation of the water column by the pile.

Estimates of pile driving sound levels in the acoustic near-field were addressed separately using a specially designed near-field model based on the wavenumber integration acoustic modeling method (Section 3.7).

3.6. Far-field rms SPL Modeling

For impulsive sound sources like impact pile driving, MONM does not directly model *rms* SPL. Nonetheless, as discussed in Section 2.3.2, SEL and *rms* SPL for impulses are related by a simple formula that depends only on the 90% energy duration of the impulses. Knowing the length of an impulse, therefore, it is possible to compute the *rms* SPL from the modeled SEL. For the current study, FWRAM was used to estimate the 90% energy length for pile driving impulses in Tappan Zee Reach by modelling synthetic pressure waveforms along a limited number of representatives transects. Range-dependent impulse-response functions were modeled at frequencies from 10 Hz to 2048 Hz in 1 Hz steps and convolved with the appropriate far-field source signatures for pile driving operations (Section 3.2) to generate synthetic pressure waveforms along each transect. These waveforms were then analyzed to determine the 90% energy length as a function of range from the pile. Three different representative transects extending to 50,000 ft (15 km) distance from the bridge were modeled using FWRAM: one transect extending upriver from pier P16/P25, one transect extending upriver from pier P25/P45, and another extending downriver from pier P25/P45.

The FWRAM pulse length predictions were used to derive a range-dependent conversion function between SEL and *rms* SPL. A smoothed function representing the mean difference between *rms* SPL and SEL was fit to the FWRAM model predictions for the three transects (Figure 14). The maximum effective pulse length was constrained on precautionary grounds to be 500 ms (corresponding to a difference of 3 dB between *rms* SPL and SEL) so that the *rms* amplitudes could not be underestimated by excessively long averaging times. The resulting range-dependent conversion factor was applied to the single-strike SEL modeling grids from MONM in order to compute *rms* SPLs from the piles. As with the SEL scenarios, *rms* SPL values were maximized over depth and rendered as two-dimensional contours on thematic maps. In addition, *rms* SPL values were decomposed into power spectral density levels (in 1/3-octave bands) at selected receiver stations and presented as plots of spectrum level versus frequency.

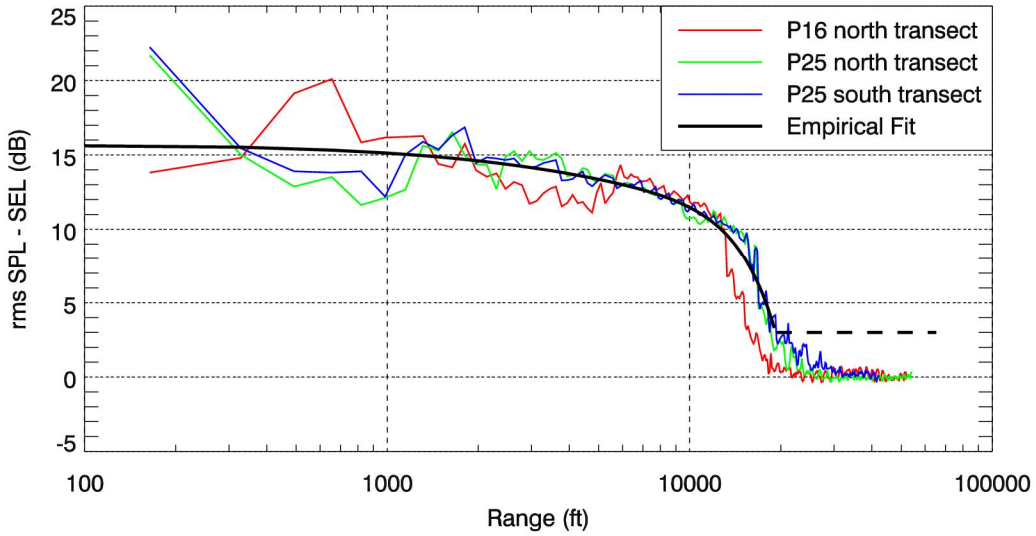

Figure 14: Conversion between SEL and *rms* SPL for pile driving in Tappan Zee Reach, as derived from three full-waveform modeling transects. The precautionary limiting value of 3 dB (corresponding 500 ms pulse length) is indicated by the dashed line.

3.7. Near-field Peak SPL Modeling

The VSTACK wavenumber integration model was used for predicting peak SPLs generated by impact pile driving. Because the wavenumber integration technique is accurate in the near-field, in VSTACK the pile was treated as a vertically distributed source extending into the sub-bottom (Figure 15). This ensured that peak SPL predictions were accurate in the near-field zone, where physical injury due to pile driving noise is most likely to occur. For the peak SPL scenarios the pile was modelled as an array of monopole elements with 3.28 ft (1 m) vertical separation. The elements representing the pile extended from 1.64 ft (0.5 m) below the water surface to the lower tip of the pile 160-300 ft (50-90 m) below the mudline. The substrate was modeled as a set of horizontally stratified acousto-elastic layers according to the site-specific geoacoustic profiles for each site (Table 4). The frequency range included in the VSTACK calculation was from 10 Hz to 2048 Hz.

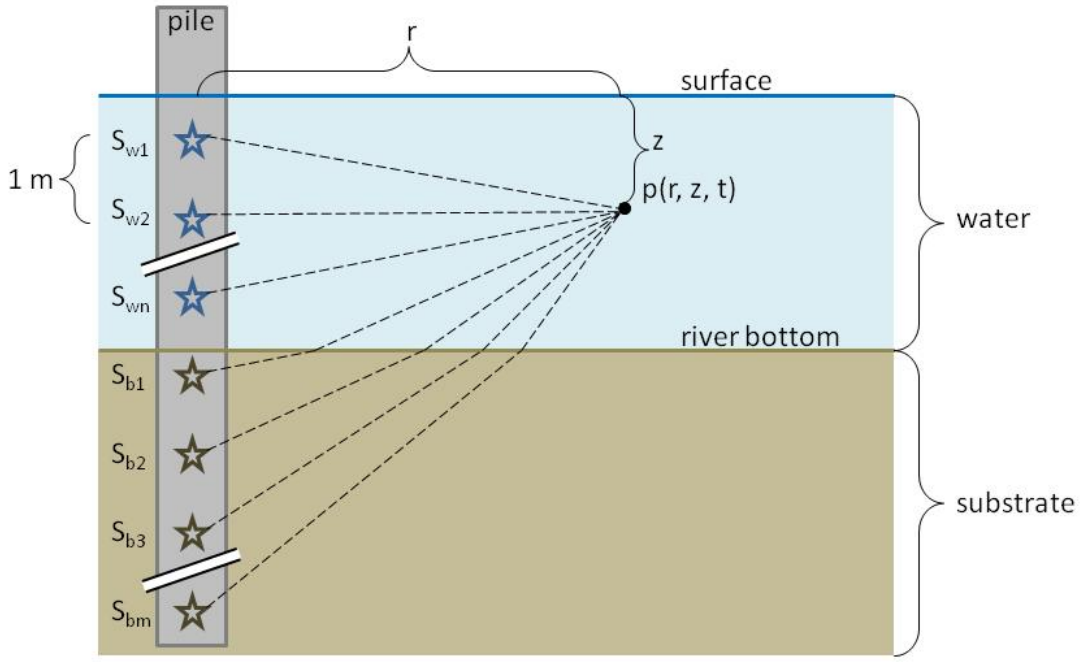

Figure 15: Diagram of VSTACK computation geometry for estimating near-field acoustic waveforms from pile driving (only direct-path rays are illustrated). Stars indicate the placement of the source elements. The vertical separation of the source elements is 1 m.

Each source element used an identical source wavelet, with time delay specified according to the vertical location of the element along the pile. Source wavelets were derived from spectral factorization of 1/3-octave band source levels for a particular pile hammer configuration (Section 3.2). The pressure wave in the water is generated by a stress wave propagating down the length of the pile with a phase speed of approximately 16,400 ft/s (5 km/s). The onset of the source wavelet for each pile element was therefore delayed according to the distance of each element along the pile divided by the phase speed of the stress wave (60 µs/ft or 200 µs/m).

In modeling sources below the mudline, the radial displacement of the pile wall was assumed to be approximately the same in the water and in the riverbed sediments. The pressure amplitude of pile elements below the mudline was therefore multiplied by the relative acoustic impedance of the sediment materials in accordance with the impedance relationship for acoustic waves (Jensen et al., 2000, §2.1). As VSTACK's handling of sub-bottom sources is limited to computing the upward-propagating acoustic wave component originating inside a uniform sediment layer, the properties of the top-most layer were used when accounting for the contribution of pile elements below the mudline. This was the most conservative assumption as it maximizes transfer of sound energy from the substrate to the water. Note that this approximation was only necessary for computing the transmission coefficient from the riverbed into the water: the full complexity of the sub-bottom layering was taken into account when considering acoustic energy from water-borne propagation paths coupling into the riverbed.

For the BMP scenarios, use of a confined bubble curtain is only expected to reduce sound emissions from the in-water segment of the pile. The frequency-dependent bubble curtain attenuation (Section 3.3) was therefore only applied to in-water pile elements. In all VSTACK based modeling the amplitudes of the bottom 10 elements of the pile were tapered to zero as a

computational requirement to prevent a sharp pressure discontinuity at the pile tip and consequent spatial "ringing". It was also necessary to scale the individual amplitudes of the source elements so that in aggregate they matched the far-field source strength of the pile. This was done by matching the received SEL predicted using VSTACK with the equivalent far-field model predictions at 1640 ft (500 m) range.

The contributions of all the pile elements were summed to generate a 250 ms long pressure-versus-time trace for each receiver point in the VSTACK output (Figure 16). Peak SPLs for each receiver were extracted directly from the modeled synthetic pressure traces. Peak SPLs were modeled at three different receiver depths (¼ water depth, ½ water depth, and ¾ water depth) to a maximum distance of 10,000 ft (3 km) from the pile. The maximum peak SPL over the three receiver depths was extracted at each range and plotted versus distance from the pile. Ranges corresponding to specific peak SPL thresholds of interest were extracted from the level versus distance plots. The ability to model finely resolved pressure spatial gradients was also the basis for particle velocity computation as discussed in the next section.

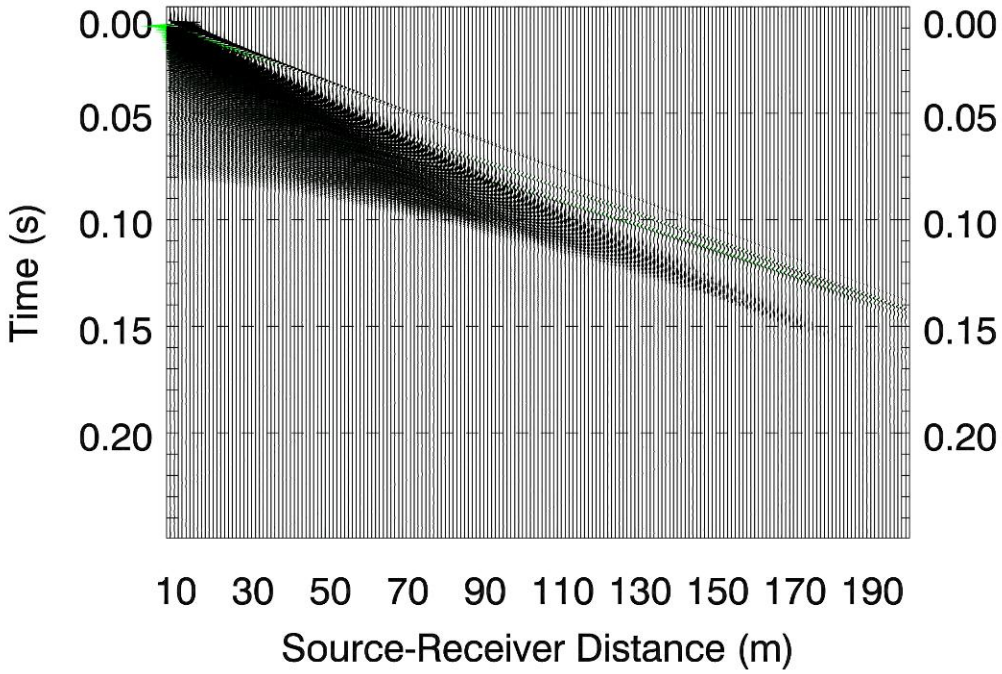

Figure 16: Time-offset plot of synthetic pressure waveforms computed using VSTACK. Black areas indicate positive acoustic pressures and green areas indicate negative acoustic pressures.

3.8. Near-field Particle Motion Modeling

VSTACK was also used to compute estimates of particle velocity for the impact pile driving scenarios. As with the peak SPL modeling, particle motion estimates were computed in the time-domain from synthetic waveform calculations. As VSTACK does not compute particle motion directly, particle velocity was derived mathematically from the numerical gradient of the

acoustic pressure. Mathematically, Euler's linearized momentum equation can be used to show that acoustic particle velocity is related to the time integral of the acoustic pressure gradient (Fahy, 1977):

$$\mathbf{v}(r,z,t) = -\int \nabla p(r,z,t) / \rho_0 dt$$

In this equation, **v** is the vector particle velocity, ρ_0 is the fluid density and p is the acoustic pressure. Numerically, the pressure gradient along a particular axis may be computed from the differential pressure between two closely spaced receivers. In the range-depth coordinate system employed by VSTACK, the numerical gradient is computed as follows:

$$\nabla p(r,z,t) \cong \frac{p(r+\Delta/2,z,t) - p(r-\Delta/2,z,t)}{\Delta}\hat{r} + \frac{p(r,z+\Delta/2,t) - p(r,z-\Delta/2,t)}{\Delta}\hat{z}$$

In this equation, r is the radial coordinate, z is the depth coordinate (the hat notation indicates the vector component along each axis), and Δ is the spatial separation between receivers. The difference approximation depends on the condition that the receiver separation, Δ, is small relative to the acoustic wavelength. The vector components of the particle velocity **v** are obtained by time-integration of the differential pressure traces, after dividing by the water density.

The VSTACK model setup for the particle velocity scenarios was identical to that for the peak SPL scenarios (Section 3.7) in terms of source treatment, frequency range and environmental model. The important difference was that the configuration for the particle velocity scenarios used a modified receiver geometry for computing the differential pressure at each range from the pile (Figure 17). The receiver separation Δ for the gradient calculation was chosen to be 0.33 ft (0.1 m). Vector particle velocity traces were computed to a maximum distance of 1,600 ft (500 m) from the pile. The particle velocity estimates were based on the amplitude of the model predicted velocity vector and were presented as plots of peak value versus range.

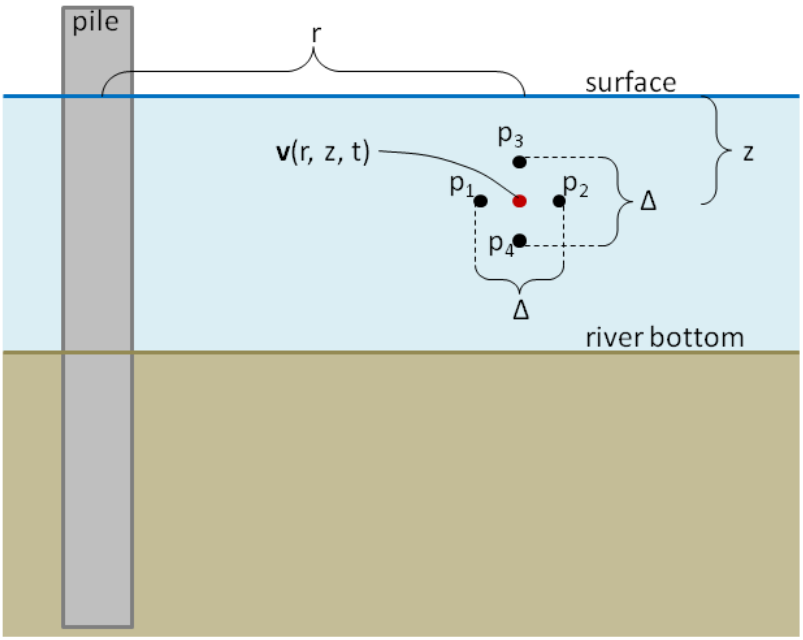

Figure 17: Diagram of VSTACK particle velocity calculation method (not to scale). The four black circles indicate the stencil points (p_1, p_2, p_3, p_4) used for computing the numerical gradient. The red circle indicates the actual computation point for the particle velocity vector.

4. Model Scenarios and Results

4.1. Overview of Model Scenarios

Model scenarios were developed with guidance from the Project's engineering team so as to represent, as accurately as possible, construction activities associated with the proposed bridge. The Project, if carried out, is expected to take 3-5 years to complete and would involve driving of approximately 1,000 steel support piles in the Hudson River. Pile driving would take place across the entire width of the river, so for the purpose of this study the bridge the span was divided into seven different foundation zones common to both proposed bridge options (dual level and single level). Piles would be driven at multiple pier locations within each foundation zone. The proposed pile diameter and hammer type are consistent inside each foundation zone, although the quantity and arrangement of the support piers would depend on the particular bridge option selected.

Seven unique source locations, distributed across the proposed bridge span, formed the basis of the impact pile driving model scenarios (Figure 18). Each source location comprised a unique set of pile driving attributes, taken from the engineering design documents: pile diameter, pile depth, hammer characteristics, and expected number of hammer strikes per pile (Table 5). Two models of hydraulic pile driving hammers are planned for use on the Project: IHC S-600 (444 kips·ft rated energy) and IHC S-750 (551 kips·ft rated energy). A unique set of geoacoustic profiles were also associated with each source location, as discussed in Section 3.4.3. It should be noted that the coordinates for each source represent an average piling location, since for each

support pier multiple piles would be installed in clusters; the small differences in source location, however, would cause only negligible changes in acoustic propagation.

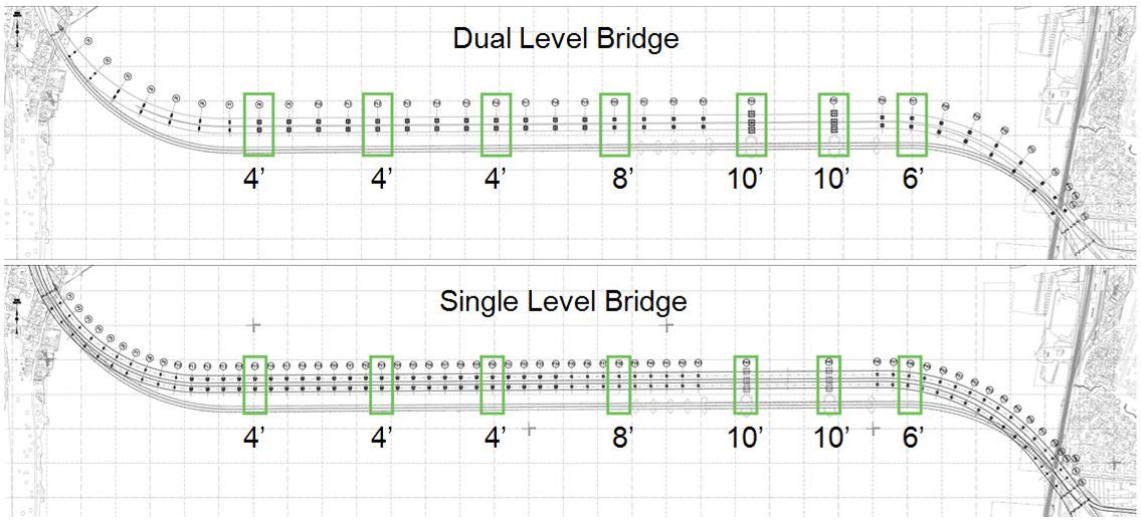

Figure 18: Impact pile driving modeling locations for dual level and single level bridge options. The annotation indicates the pile diameter at each source location.

Table 5. Modeling source locations for impact pile driving, and pile driving characteristics.

Pile ø	Pier Number Dual	Pier Number Single	Pile Depth Dual	Pile Depth Single	Found-ation Zone	Hammer Model and Energy	Strike Count	*Coordinates (NY State Plane East)* Easting (feet)	Northing (feet)
4'	P8	P15	300'	300'	2	IHC S-600, 444 kips·ft,	3800	655,012	815,695
4'	P12	P23	300'	300'	3	IHC S-600, 444 kips·ft,	3800	656,733	815,643
4'	P16	P30	300'	300'	3	IHC S-600, 444 kips·ft,	3800	658,453	815,662
8'	P20	P38	210'	210'	4	IHC S-750 551 kips·ft	2100	660,174	815,672
10'	P24	P44	280'	240'	5	IHC S-750, 551 kips·ft	2900	662,163	815,685
10'	P25	P45	280'	240'	5	IHC S-750, 551 kips·ft	2900	663,367	815,695
6'	P27	P48	160'	160'	6	IHC S-750, 551 kips·ft	1000	664,490	815,687

Two different kinds of pile driving scenarios were modeled for the current study:

1. Cumulative scenarios that considered cumulative sound exposure (cSEL) from a full day of construction activities. Estimates from cumulative scenarios are intended for evaluating physiological impacts on fishes due to pile driving activities.

2. Single-strike scenarios that considered the acoustic footprint of a single impulse from a pile driving hammer. Estimates from single-strike scenarios are intended for evaluating both physiological and behavioral impacts on fishes due to pile driving activities.

Representative combinations of piling activities for the cumulative scenarios were devised through consultations between the EIS team and the Project engineering team. Construction schedules for both proposed bridge options involve hundreds of days of pile placement. On a single day, different sizes and quantities of piles may be driven at multiple locations. A set of daily piling combinations was selected from the proposed schedules based on a specific set of requirements:

1. To translate the schedules into a limited number of locations and modeling runs,
2. To include ecologically important scenarios,
3. To focus on the main span, which encompasses the river's migratory channel.

The pile driving acoustic footprint is likely to be largest when: (1) large diameter piles are being driven and (2) multiple piles are driven during the same day. The Project's engineering team developed a series of daily maximum pile driving combinations to be considered in establishing the proposed hydroacoustic modeling framework. From these pile driving combinations, three maximum case scenarios were selected for each bridge option that reflected conditions of greatest ecological interest (Table 6). Three additional pile driving scenarios were selected for each bridge options so as to generate acoustic modeling results for typical daily pile driving events, as opposed to the maximum events. Each of the maximum and typical cases was modeled with and without BMPs, for a total of 24 cumulative modeling cases. Eight of the model scenarios, however, were common to the single level and dual level bridge options. Thus, a total of 16 unique cumulative model scenarios were considered. Outputs from the corresponding model runs were expressed in terms of cumulative sound exposure level (cSEL).

Table 6. Quantities, sizes, and locations of impact pile driving for cumulative (cSEL) modeling scenarios. All scenarios listed in the table were modeled with and without BMPs.

Pile Size	4'	4'	4'	8'	10'	10'	6'
Pier Number Dual	*P8*	*P12*	*P16*	*P20*	*P24*	*P25*	*P27*
Max Case 1					2	2	
Max Case 2A		3		3			4
Max Case 3	3						4
Pier Number Single	*P15*	*P23*	*P30*	*P38*	*P44*	*P45*	*P48*
Max Case 1					2	2	
Max Case 2B		3		3			4
Max Case 3	3						4
Pier Number Dual	*P8*	*P12*	*P16*	*P20*	*P24*	*P25*	*P27*
Typical Case 1					1	1	
Typical Case 2A				2			2
Typical Case 3		2	2				
Pier Number Single	*P15*	*P23*	*P30*	*P38*	*P44*	*P45*	*P48*
Typical Case 1					1	1	
Typical Case 2B		2		2			2
Typical Case 3		2	2				

Single-strike pile driving events were modeled at four different locations across the bridge span (Figure 19). Locations and pile driving characteristics for the single-strike cases were common to both bridge options. The cases were modeled both with and without BMPs, for a total of eight single-strike scenarios. These scenarios were modeled by means of three different hydroacoustic models (Section 3.1), yielding results in multiple acoustic metrics. The following metrics relevant to physiological and behavioral impact assessment were computed: peak SPL (physiological and behavioral), single-strike SEL (physiological), *rms* SPL (behavioral), SPL power spectral density (behavioral), and particle velocity (behavioral). SPL power spectral density levels for the single-strike scenarios were computed in 1/3-octave bands at 14 fixed locations (virtual receiver stations) in Tappan Zee Reach (Figure 19). Receiver stations were grouped according to their position relative to the river channel: WS (west shallows), WC (west channel), SC (south channel), and CC (central channel).

In total, 24 distinct pile driving scenarios were modeled by multiple methods to obtain acoustic data for assessing the physiological and behavioral impacts of pile driving on Hudson River aquatic resources (Table 7). The following report sections provide an overview and samples of results for the various model scenarios and outputs. Detailed results for all 24 scenarios are provided in an appendix to this report. Results from the cumulative scenarios (1-16) are presented in Section 4.2 and Appendix A. Results from the single-strike scenarios (17-24) are presented in Sections 4.3-4.6 and Appendices B-D.

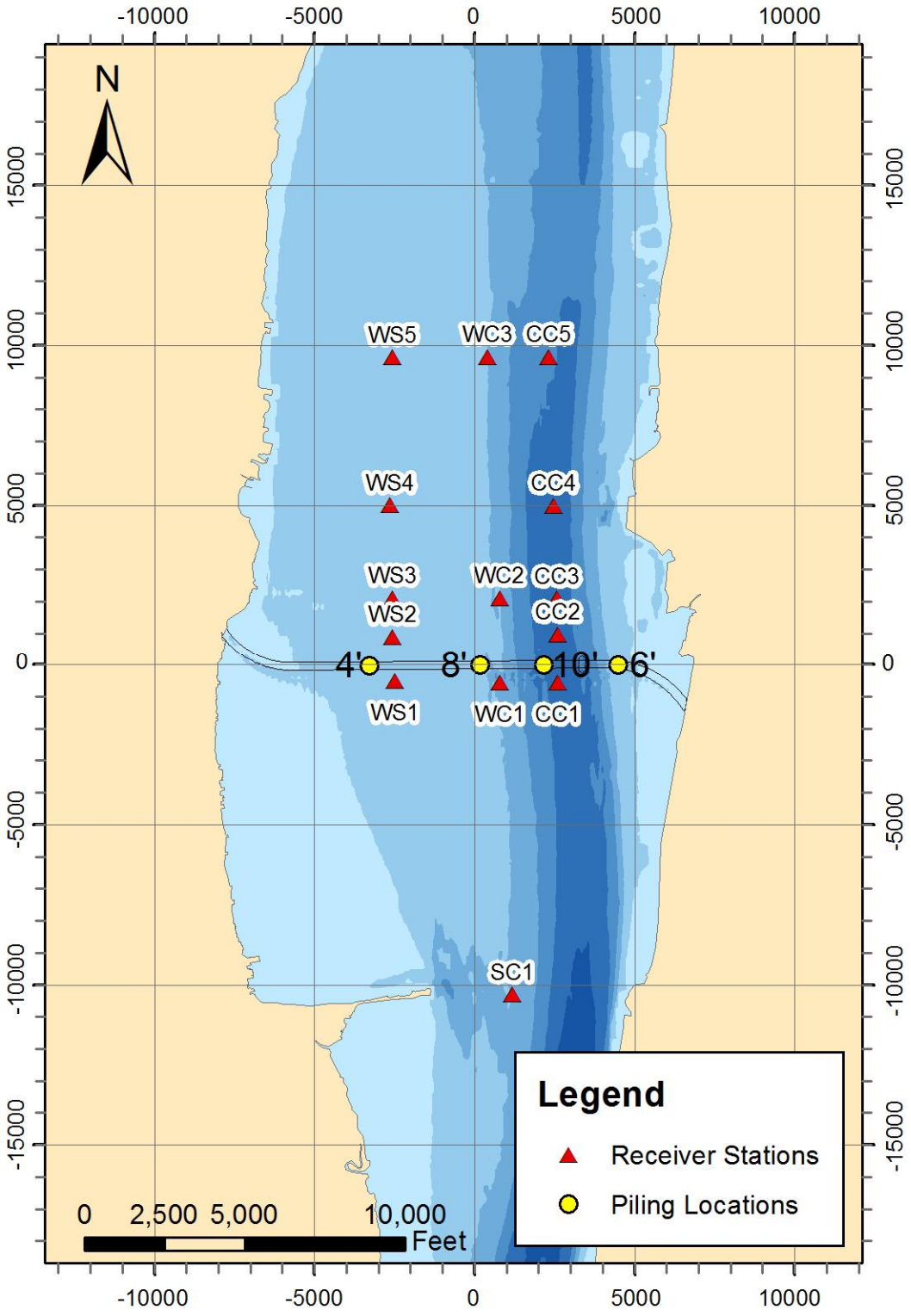

Figure 19: Impact pile driving locations for single-strike model scenarios (yellow circles) and receiver stations for reporting of PSD levels from impact pile driving (red triangles). Map grid shows coordinates in feet, relative to the bridge center.

Table 7. List of all impact pile driving model scenarios. "X"s indicate the metrics that were modeled for each scenario.

Scenario				Metric				
Number	Bridge Type	BMPs	Description	*Cumulative Physiological* cSEL (§4.2, App. A)	*Single Strike Physiological* SEL (§4.3, App. B)	*Single Strike Physiol./Behav.* Peak SPL (§4.4, App. C)	*Single Strike Behavioral rms* SPL (§4.5, App. D)	*Single Strike Behavioral* Particle Velocity (§4.6)
1	Dual/Single	No	Max Case 1	X				
2	Dual	No	Max Case 2A	X				
3	Dual/Single	No	Max Case 3	X				
4	Single	No	Max Case 2B	X				
5	Dual/Single	Yes	Max Case 1	X				
6	Dual	Yes	Max Case 2A	X				
7	Dual/Single	Yes	Max Case 3	X				
8	Single	Yes	Max Case 2B	X				
9	Dual/Single	No	Typical Case 1	X				
10	Dual	No	Typical Case 2A	X				
11	Dual/Single	No	Typical Case 3	X				
12	Single	No	Typical Case 2B	X				
13	Dual/Single	Yes	Typical Case 1	X				
14	Dual	Yes	Typical Case 2A	X				
15	Dual/Single	Yes	Typical Case 3	X				
16	Single	Yes	Typical Case 2B	X				
17	Dual/Single	No	Single Strike 4'		X	X	X	X
18	Dual/Single	No	Single Strike 6'		X	X	X	X
19	Dual/Single	No	Single Strike 8'		X	X	X	
20	Dual/Single	No	Single Strike 10'		X	X	X	X
21	Dual/Single	Yes	Single Strike 4'		X	X	X	
22	Dual/Single	Yes	Single Strike 6'		X	X	X	
23	Dual/Single	Yes	Single Strike 8'		X	X	X	
24	Dual/Single	Yes	Single Strike 10'		X	X	X	

4.2. Cumulative SEL Metric

4.2.1. cSEL contour areas

For the cumulative scenarios (1-16), three-dimensional spatial grids of cSEL were computed using MONM according to the methodology described in Section 3.5. The cSEL model results were then converted to maximum-over-depth contours and rendered on thematic maps (Appendix A). Contours were rendered at the following seven cSEL threshold levels:

- 207 dB re 1 µPa^{2}s
- 204 dB re 1 µPa^{2}s
- 201 dB re 1 µPa^{2}s
- 197 dB re 1 µPa^{2}s
- 194 dB re 1 µPa^{2}s
- 187 dB re 1 µPa^{2}s
- 183 dB re 1 µPa^{2}s

The total surface area ensonified at levels above each cSEL threshold was computed from the model output for each scenario and reported (in units of 1,000 ft^2) in Table 8. It should be stressed here that cSEL contours must not be interpreted as representing a static picture of the sound field in Tappan Zee Reach. The contours in fact grow steadily around the piling activity as multiple piles are driven at each pier over the course of a day, and the cSEL contours and surface areas presented in the maps and tables represent the maximum extent of a dosage metric at the end of a complete working day.

The following subsections present example cSEL contour maps for four selected scenarios (2, 4, 6, and 8). Sound level contour maps for all 16 cumulative SEL scenarios are presented in the appendix.

Table 8. Area ensonified above the specified cSEL threshold levels (units of 1,000 ft^2) for the cumulative model scenarios.

Scenario						*Area of cSEL contour (1,000 ft^2)*						
Number	Description	Bridge Type	Activity	BMPs	Map Reference	207 dB re 1 µPa^{2}s	204 dB re 1 µPa^{2}s	201 dB re 1 µPa^{2}s	197 dB re 1 µPa^{2}s	194 dB re 1 µPa^{2}s	187 dB re 1 µPa^{2}s	183 dB re 1 µPa^{2}s
1	Max Case 1	Dual/ Single	2×10 ft ø piles @ P24/P44 2×10 ft ø piles @ P25/P45	No	A1.1	25,331	31,776	40,000	52,773	64,843	98,347	123,380
2	Max Case 2A	Dual	3×8 ft ø piles @ P20 4×6 ft ø piles @ P27	No	A3.2	6,359	9,942	13,057	23,083	29,503	50,897	65,529
3	Max Case 3	Dual/ Single	3×4 ft ø piles @ P8/P15 4×6 ft ø piles @ P27/P48	No	A1.3	1,541	2,192	2,932	5,860	8,561	20,425	29,970
4	Max Case 2B	Single	3×4 ft ø piles @ P23 3×8 ft ø piles @ P38 4×6 ft ø piles @ P48	No	A1.2	6,491	10,134	14,153	26,550	33,901	57,379	72,259
5	Max Case 1	Dual/ Single	2×10 ft ø piles @ P24/P44 2×10 ft ø piles @ P25/P45	Yes	A2.1	10,528	14,777	19,111	30,008	37,338	60,361	77,708
6	Max Case 2A	Dual	3×8 ft ø piles @ P20 4×6 ft ø piles @ P27	Yes	A4.2	1,495	2,394	3,735	7,200	10,808	26,333	36,608
7	Max Case 3	Dual/ Single	3×4 ft ø piles @ P8/P15 4×6 ft ø piles @ P27/P48	Yes	A2.3	90	141	427	1,306	1,980	5,151	10,164
8	Max Case 2B	Single	3×4 ft ø piles @ P23 3×8 ft ø piles @ P38 4×6 ft ø piles @ P48	Yes	A2.2	1,526	2,443	3,803	7,316	10,972	29,856	40,846
9	Typical Case 1	Dual/ Single	1×10 ft ø piles @ P24/P44 1×10 ft ø piles @ P25/P45	No	A1.4	17,704	25,315	31,752	42,330	52,731	82,355	102,870
10	Typical Case 2A	Dual	2×8 ft ø piles @ P20 2×6 ft ø piles @ P27	No	A3.5	4,651	7,582	10,860	16,350	25,258	44,073	57,345
11	Typical Case 3	Dual/ Single	2×4 ft ø piles @ P12/P23 2×4 ft ø piles @ P16/P30	No	A1.6	217	297	545	4,106	6,843	11,842	17,399
12	Typical Case 2B	Single	2×4 ft ø piles @ P23 2×8 ft ø piles @ P38 2×6 ft ø piles @ P48	No	A1.5	4,760	7,729	11,168	18,886	29,190	50,174	64,833
13	Typical Case 1	Dual/ Single	1×10 ft ø piles @ P24/P44 1×10 ft ø piles @ P25/P45	Yes	A2.4	6,782	10,516	14,764	22,195	29,976	50,060	65,710
14	Typical Case 2A	Dual	2×8 ft ø piles @ P20 2×6 ft ø piles @ P27	Yes	A4.5	213	1,945	2,785	5,174	8,583	20,968	31,475
15	Typical Case 3	Dual/ Single	2×4 ft ø piles @ P12/P23 2×4 ft ø piles @ P16/P30	Yes	A2.6	53	79	111	181	255	4,291	7,542
16	Typical Case 2B	Single	2×4 ft ø piles @ P23 2×8 ft ø piles @ P38 2×6 ft ø piles @ P48	Yes	A2.5	241	1,982	2,838	5,266	8,717	23,570	35,587

4.2.2. Single Level Bridge: No BMPs applied

Figure 20 shows cSEL contours for Scenario 4: Max Case 2B without BMPs. Refer to Appendix A.1 for the complete set of cSEL maps for the single level bridge without BMPs.

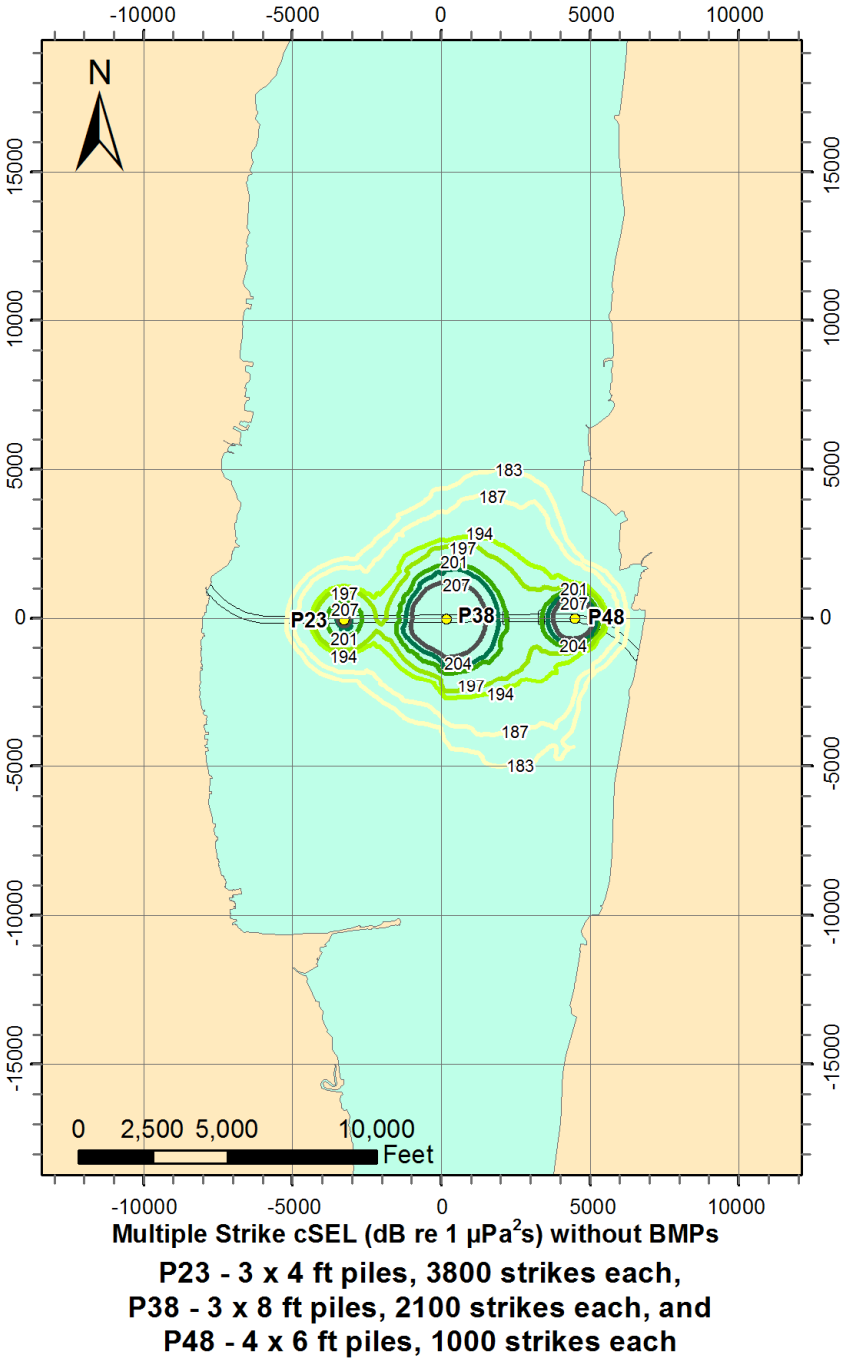

Figure 20: cSEL contour map for Scenario 4: Max Case 2B without BMPs.

4.2.3. Single Level Bridge: BMPs applied

Figure 21 shows cSEL contours for Scenario 8: Max Case 2B with BMPs. Refer to Appendix A.2 for the complete set of cSEL maps for the single level bridge with BMPs.

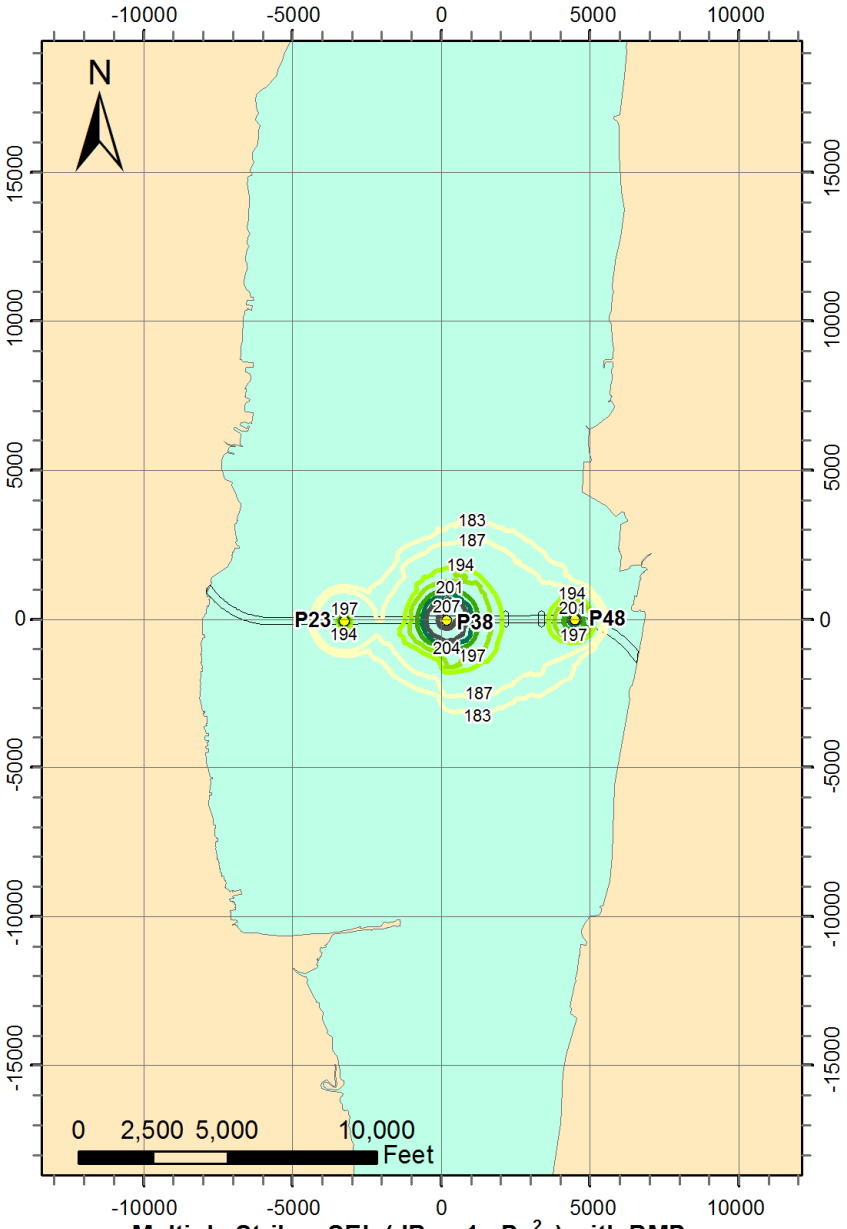

Multiple Strike cSEL (dB re 1 µPa^{2}s) with BMPs

P23 - 3 x 4 ft piles, 3800 strikes each,
P38 - 3 x 8 ft piles, 2100 strikes each, and
P48 - 4 x 6 ft piles, 1000 strikes each

Figure 21: cSEL contour map for Scenario 8: Max Case 2B with BMPs.

4.2.4. Dual Level Bridge: No BMPs applied

Figure 22 shows cSEL contours for Scenario 2: Max Case 2A without BMPs. Refer to Appendix A.3 for the complete set of cSEL maps for the dual level bridge without BMPs.

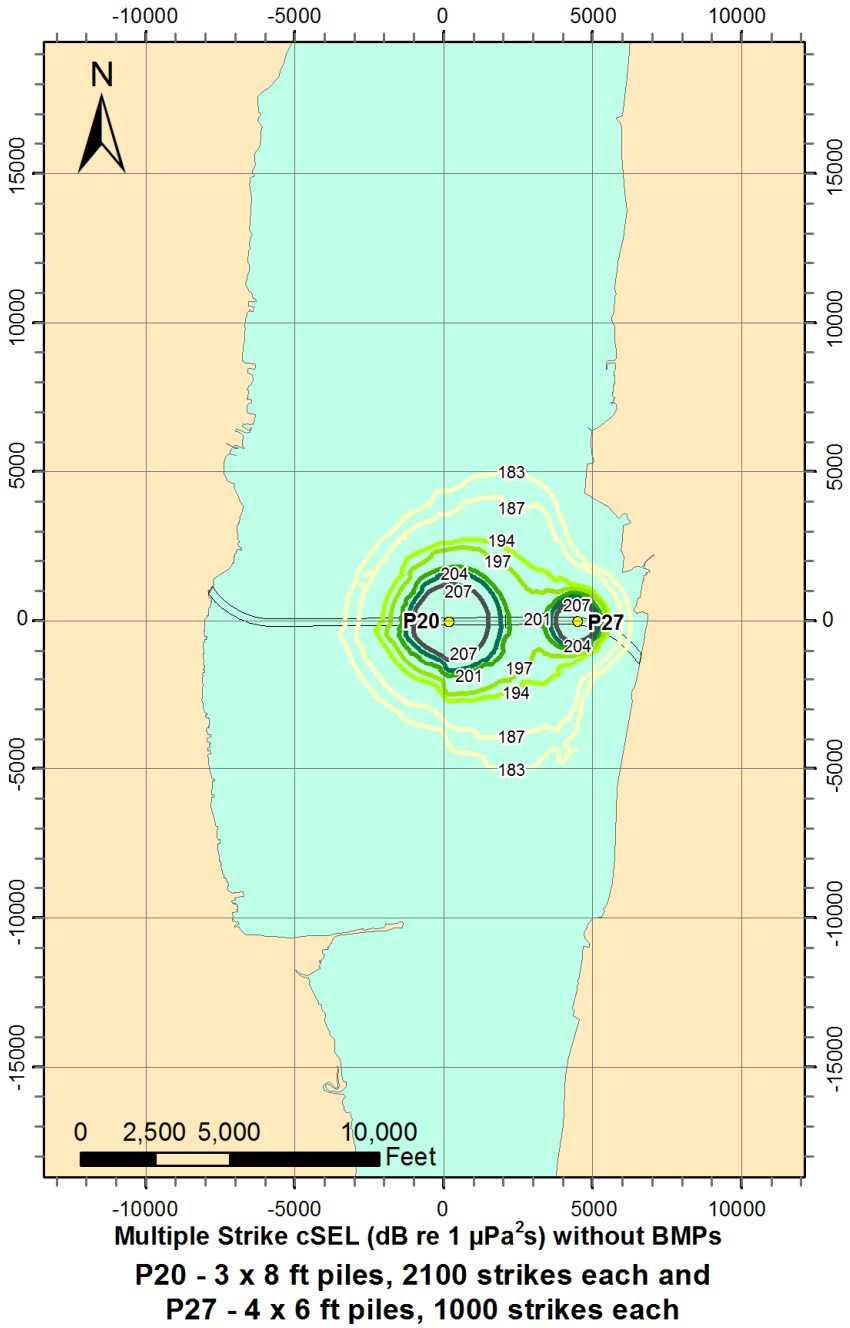

Figure 22: cSEL contour map for scenario 2: Max Case 2A without BMPs.

4.2.5. Dual Level Bridge: BMPs applied

Figure 23 shows cSEL contours for Scenario 6: Max Case 2A with BMPs. See Appendix A.4 for the complete set of cSEL maps for the dual level bridge without BMPs.

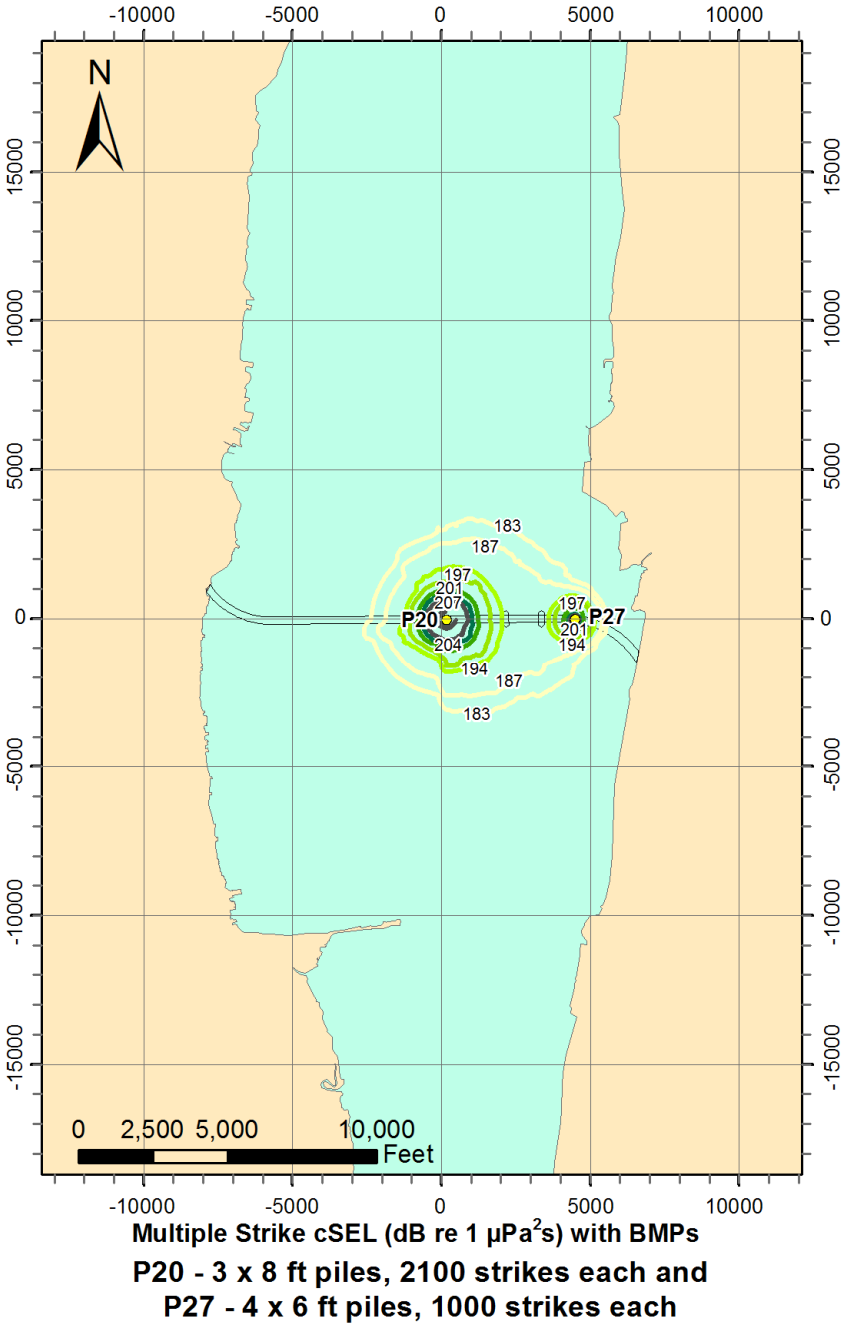

Figure 23: cSEL contour map for Scenario 6: Max Case 2B with BMPs.

4.3. Single Strike SEL Metric

For the single strike scenarios (17-24), three-dimensional spatial grids of single-impulse SEL were computed using MONM according to the methodology described in Section 3.5. The SEL model results were then converted to maximum-over-depth contours and rendered on thematic maps (Appendix B). Contours were rendered at the following six SEL threshold levels:

- 193dB re 1 μPa^2s
- 187 dB re 1 μPa^2s
- 181 dB re 1 μPa^2s
- 175 dB re 1 μPa^2s
- 169 dB re 1 μPa^2s
- 163 dB re 1 μPa^2s

Unlike the cSEL results, the SEL contours represent a snapshot of the acoustic energy footprint temporarily introduced into the river during a single blow of the pile driving hammer acting at one pier location. The SEL contours are intended to present average per-strike sound levels for the specified pile driving activity. The intensity of sound emitted during impact pile driving fluctuates over time, to some degree, as varying soil resistance conditions are encountered (Robinson et al., 2007).

The following subsections present examples of single strike SEL contour maps for two selected scenarios (18 and 22). Sound level contour maps for all eight single-strike SEL scenarios are presented in the appendix.

4.3.1. Single and Dual Level Bridge: No BMPs Applied

Figure 24 shows single strike SEL contours for Scenario 18: 6 ft diameter pile at P27/P48 without BMPs. Refer to Appendix B.1 for the complete set of single strike SEL maps without BMPs.

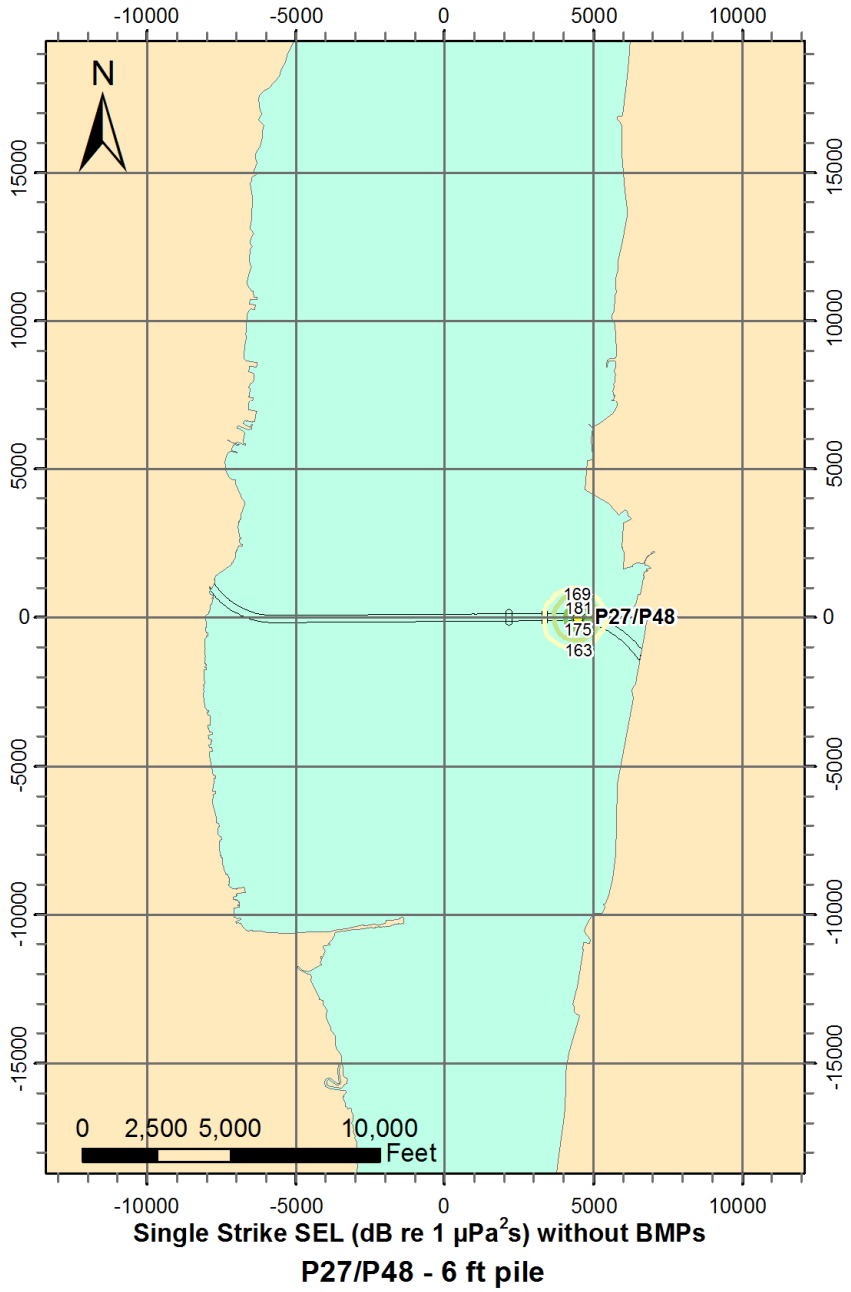

Figure 24: Single strike SEL contour map for Scenario 18: 6 ft pile at P27/P48 without BMPs.

4.3.2. Single and Dual Level Bridge: BMPs Applied

Figure 25 shows single strike SEL contours for Scenario 22: 6 ft diameter pile at P27/P48 with BMPs. Refer to Appendix B.2 for the complete set of single strike SEL maps with BMPs.

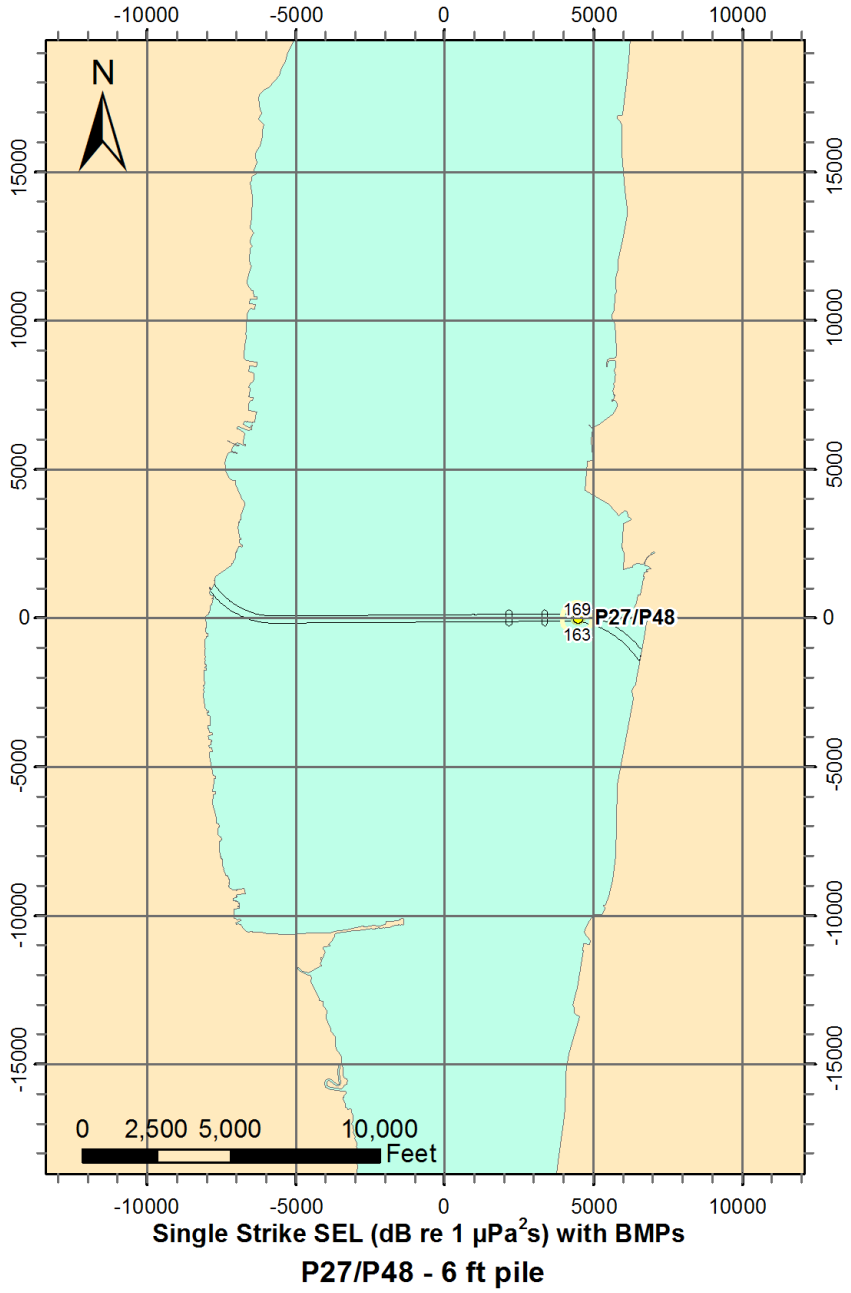

Figure 25: Single strike SEL contour map for Scenario 22: 6 ft pile at P27/P48 with BMPs.

4.4. Peak SPL Metric

Peak SPLs for the single strike scenarios (17-24) were computed using VSTACK according to the methodology described in Section 3.7. Peak SPLs were modeled for 4, 6, 8, and 10 ft piles with and without BMPs. Estimates from the VSTACK model are valid in the near-field zone and explicitly account for sound transmitted from the substrate into the water including vibration of the riverbed interface induced by the pile. The modeling results were used to generate curves of peak SPL, maximized over three depths, versus distance from the pile (Figure 26 and Figure 27). Distances corresponding to specific peak SPL thresholds, from 214 dB to 184 dB re 1 µPa in 6 dB steps, were extracted from the level versus range curves and are shown in Table 9.

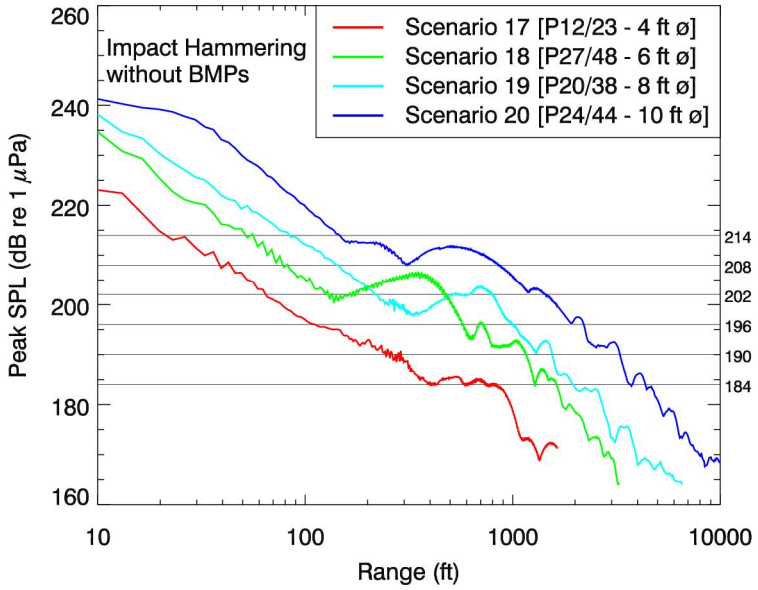

Figure 26: Peak SPL versus distance for scenarios 17-20, impact hammering of 4, 6, 8, and 10 ft diameter piles without BMPs. Gray lines indicate peak SPL thresholds from 214 dB to 184 dB re 1 µPa in 6 dB steps.

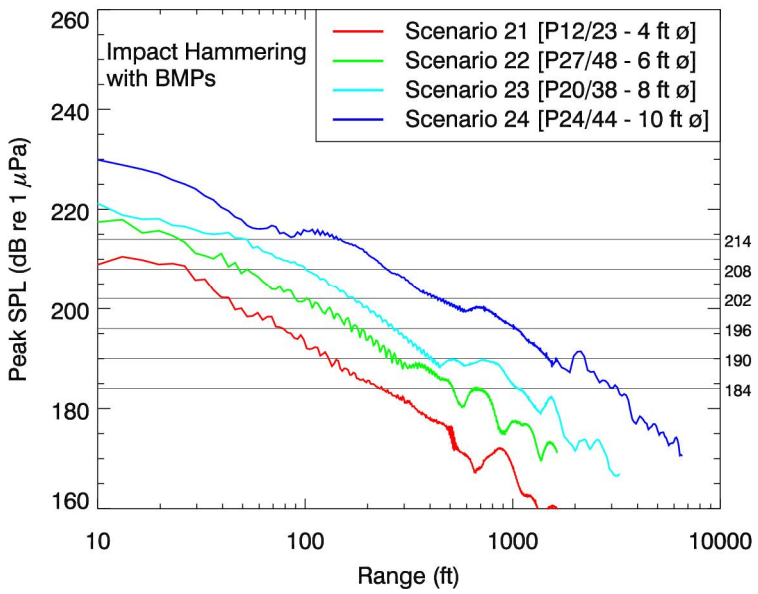

Figure 27: Peak SPL versus distance for scenarios 21-24, impact hammering of 4, 6, 8, and 10 ft diameter piles with BMPs. Gray lines indicate peak SPL thresholds from 214 dB to 184 dB re 1 µPa in 6 dB steps.

Table 9. Distances to peak level thresholds for impact hammering 4, 6, 8, and 10 ft diameter piles without BMPs.

Scenario	Pile Diameter (ft)	*Distance to peak SPL threshold (ft)* 214 dB re 1 µPa	208 dB re 1 µPa	202 dB re 1 µPa	196 dB re 1 µPa	190 dB re 1 µPa	184 dB re 1 µPa
Single and Dual Level Bridge without BMPs							
17	4	21	43	64	111	289	834
18	6	56	82	479	718	1,157	1,626
19	8	84	144	800	1,007	1,553	1,949
20	10	146	861	1,447	2,201	3,289	4,364
Single and Dual Level Bridge with BMPs							
21	4	4	26	42	77	129	234
22	6	24	47	102	178	273	686
23	8	51	100	171	265	407	1,061
24	10	148	247	446	1,043	2,226	3,210

4.5. rms SPL Metric: Pile Driving Scenarios

For the single strike impact pile driving scenarios (17-24), *rms* SPL was computed using MONM and FWRAM according to the methodology described in Section 3.6. The *rms* SPL model results were converted to maximum-over-depth contours, in 6 dB steps from 198 dB to 138 dB re 1 µPa, and rendered on thematic maps (Appendix C). Example contour maps of *rms* SPL for two selected scenarios (18 and 22) are presented below. Additionally, *rms* SPL values were extracted along the radial of maximum sound propagation for each scenario. The resulting functions of *rms* SPL versus range were plotted down to the 80 dB re 1 µPa threshold (Figure 28 and Figure 29). The threshold of audibility is roughly defined by the range at which the *rms* SPL falls below the ambient background SPL.

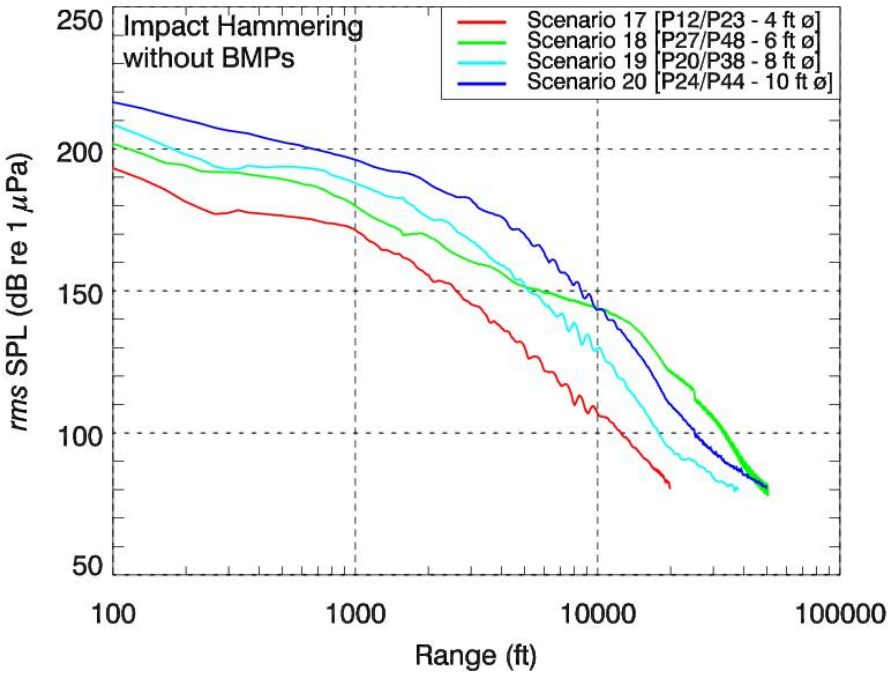

Figure 28: Max-over-depth *rms* SPL as a function of distance along the radial of maximum sound propagation (Scenario 17-20, impact pile driving without BMPs).

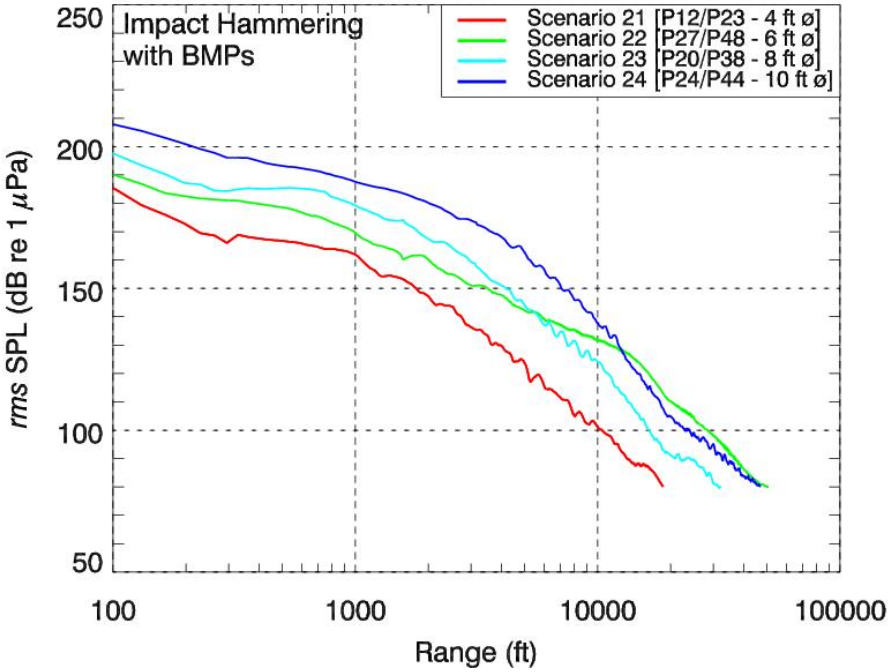

Figure 29: Max-over-depth *rms* SPL as a function of distance along the radial of maximum sound propagation (Scenario 21-24, impact pile driving with BMPs).

4.5.1. Single and Dual Level Bridge: No BMPs Applied

Figure 30 shows *rms* SPL contours for Scenario 18: 6 ft diameter pile at P27/P48 without BMPs. Refer to Appendix C.1 for the complete set of single strike *rms* SPL contour maps without BMPs (scenarios 17-20).

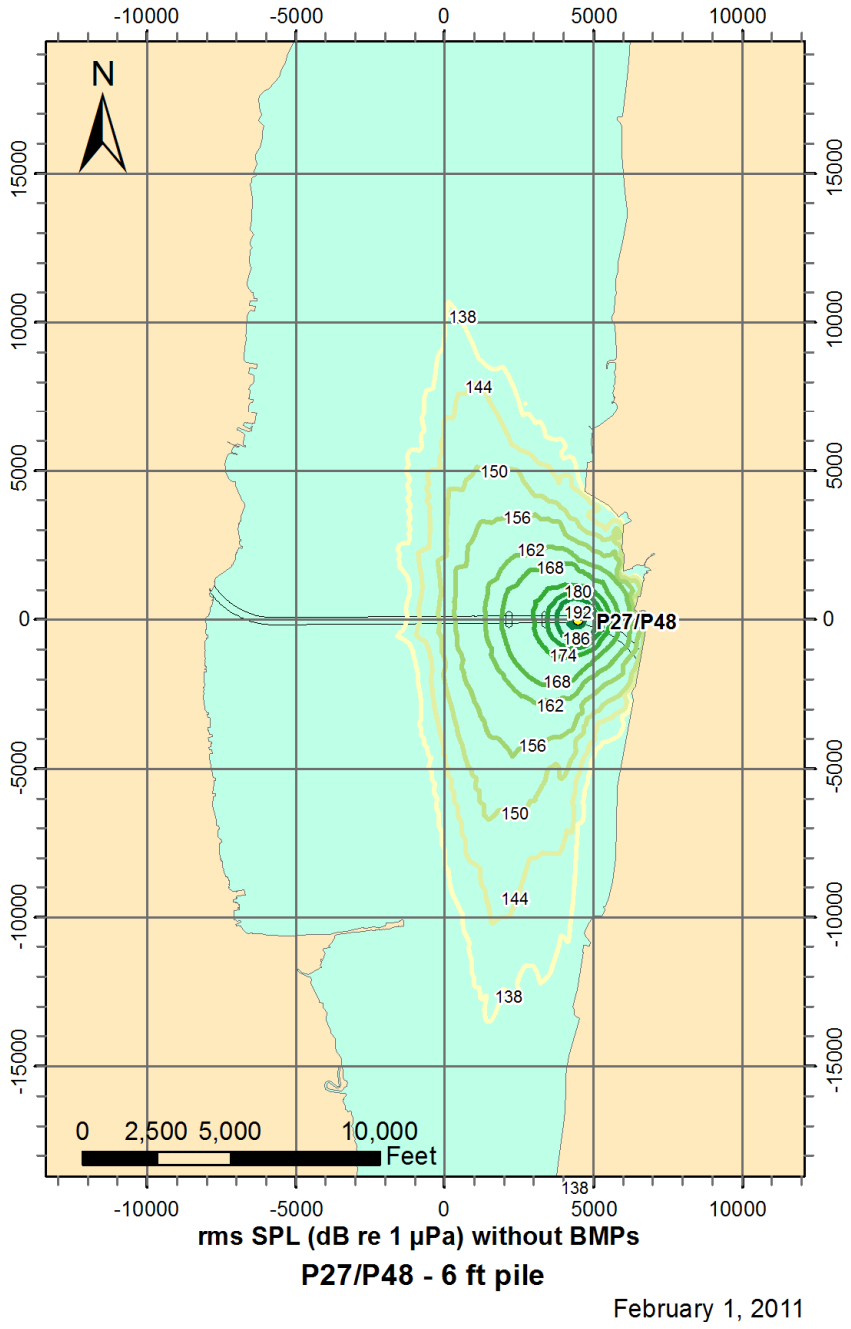

Figure 30: *rms* SPL contour map for Scenario 18: 6 ft pile at P27/P48 without BMPs.

4.5.2. Single and Dual Level Bridge: BMPs Applied

Figure 31 shows *rms* SPL contours for Scenario 22: 6 ft diameter pile at P27/P48 with BMPs. Refer to Appendix C.2 for the complete set of single strike *rms* SPL contour maps with BMPs (scenarios 21-24).

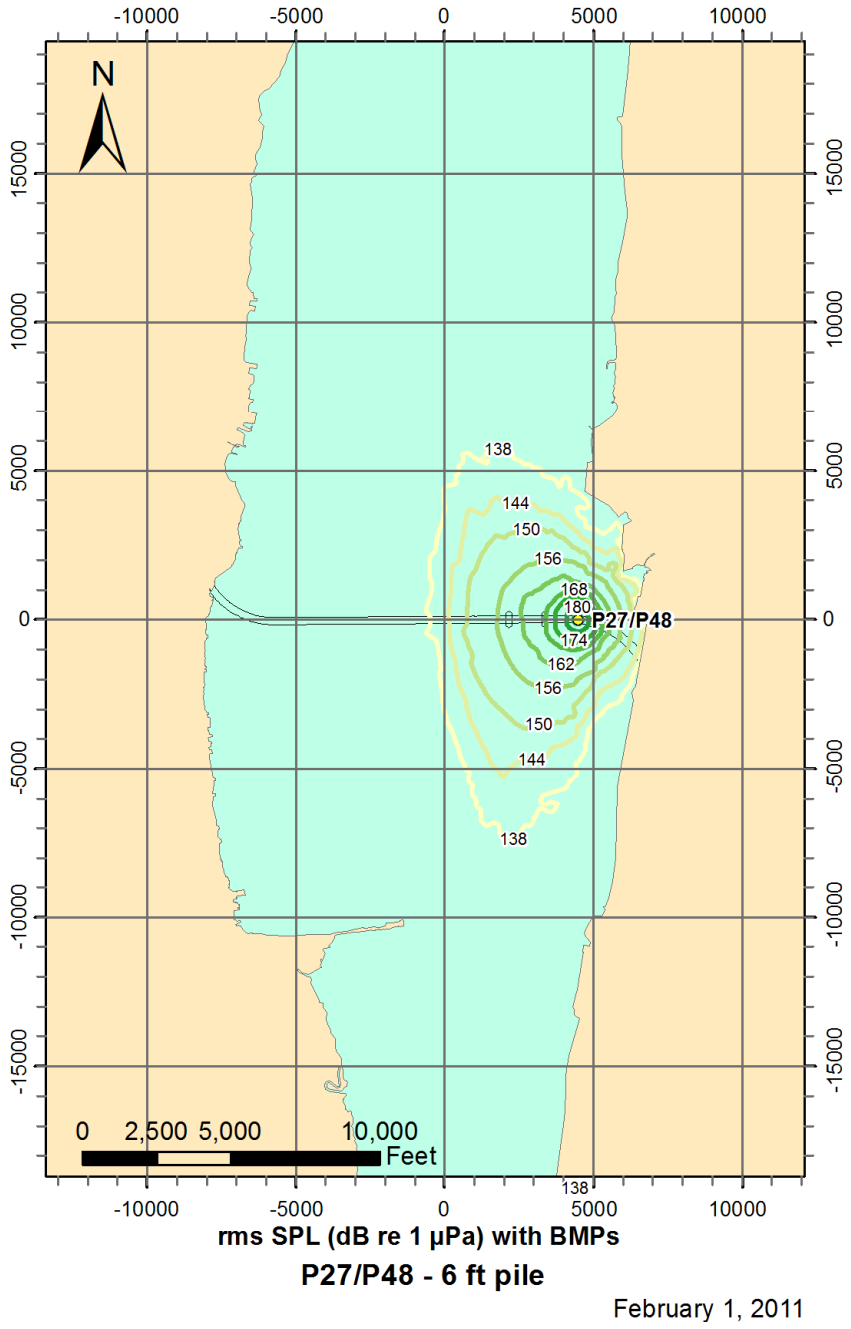

Figure 31: *rms* SPL contour map for Scenario 22: 6 ft pile at P27/P48 with BMPs.

4.6. Sound Power Spectral Density Levels

PSD levels for the single strike scenarios (17-24) were calculated at 14 fixed receiver stations (Figure 19). PSD levels were extracted at the depth of the maximum broadband level and presented as plots and tables of spectrum level versus frequency (Appendix D). Examples of PSD plots for two selected scenarios (18 and 22) are presented below (Figure 32 and Figure 33).

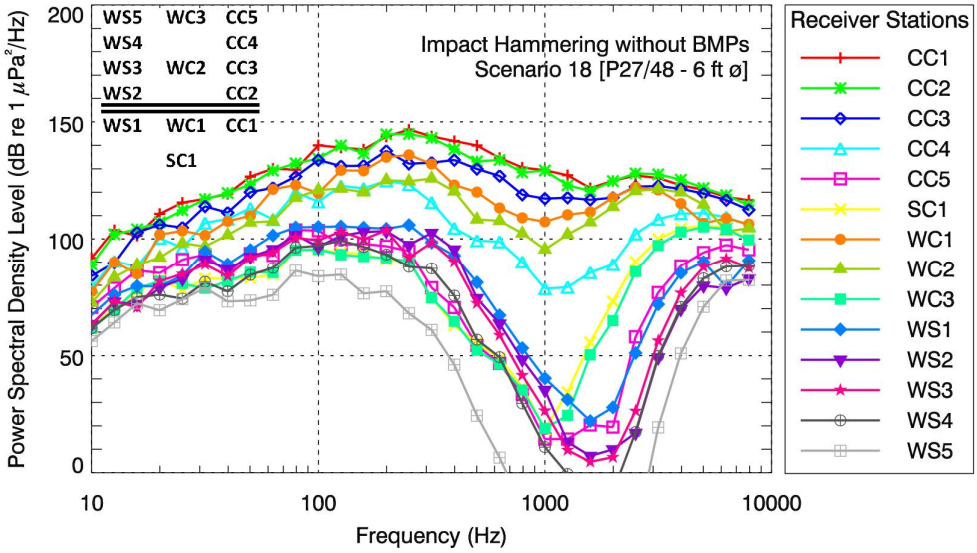

Figure 32: Power spectral density levels (at the depth where broadband level is highest) for Scenario 18: 6 ft diameter pile at P27/P48 without BMPs. Plot annotation shows receiver locations in relation to the bridge span (not to scale). See Figure 19 for a full scale map showing the locations of the receiver stations.

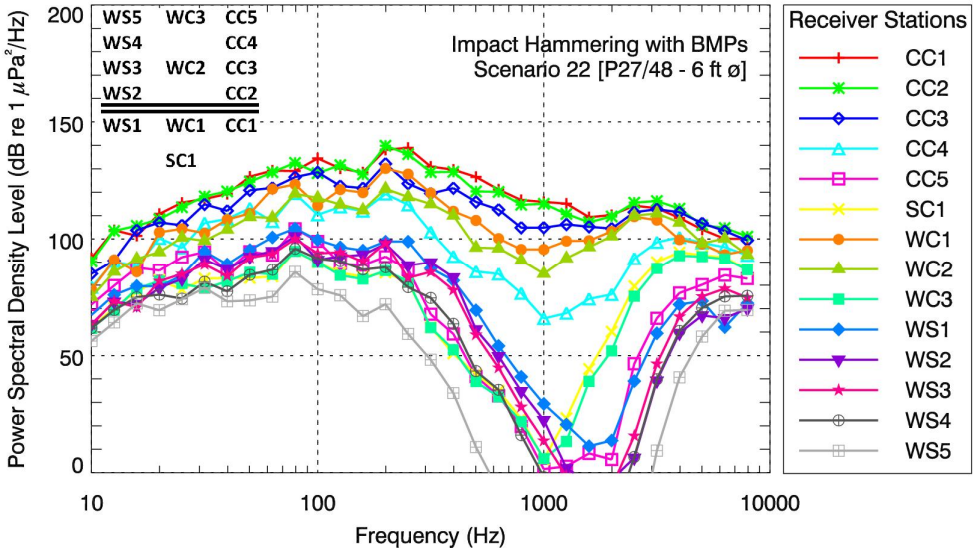

Figure 33: Power spectral density levels (at the depth where broadband level is highest) for Scenario 22: 6 ft diameter pile at P27/P48 with BMPs. Plot annotation shows receiver locations in relation to the bridge span (not to scale). See Figure 19 for a full scale map showing the locations of the receiver stations.

4.7. Single Strike Particle Motion

4.7.1. Single and Dual Level Bridge: No BMPs Applied

Peak particle velocity for three single strike scenarios (17, 18, and 20) was computed using VSTACK according to the methodology described in Section 3.8. Particle velocity was modeled for 4, 6, and 10 ft piles without BMPs only. Predictions of the VSTACK model are valid in the near-field zone and explicitly account for sound transmitted from the substrate into the water including vibration of the riverbed interface induced by the pile. The results of the modeling were used to generate curves of peak particle velocity versus distance from the pile (Figure 34). Peak particle velocity levels for each scenario were extracted from the level versus range curves at selected distances (Table 10).

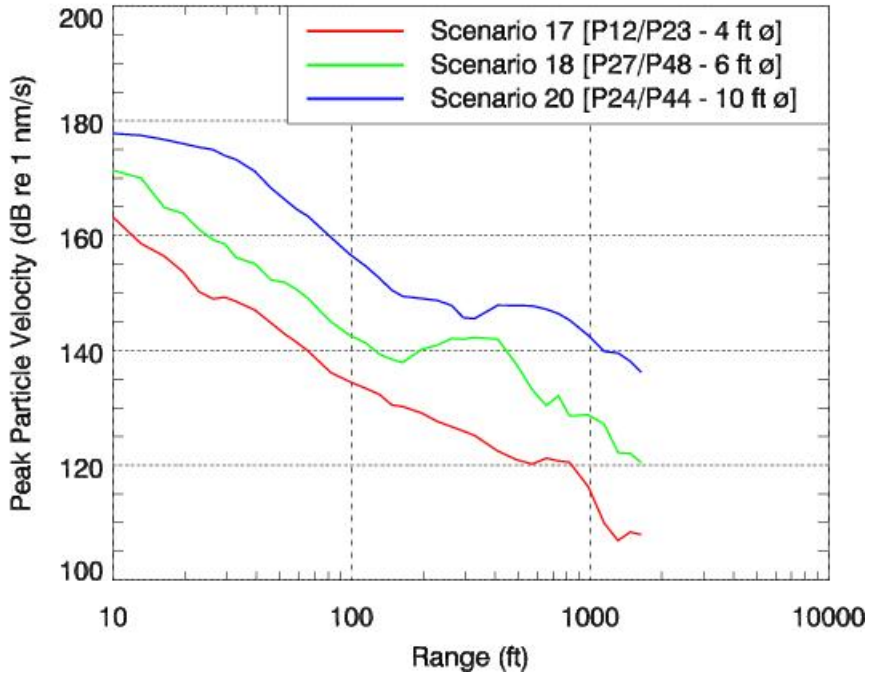

Figure 34. Peak particle velocity versus range for Scenarios 17, 18, and 20: impact hammering of 4, 6, and 10 ft piles without BMPs.

Table 10. Peak particle velocity at various distances from the source for Scenarios 17, 18, and 20: impact hammering of 4, 6, and 10 ft piles without BMPs.

		Peak particle velocity at specified range (dB re 1 nm/s)						
Scenario Number	Activity	10 ft	25 ft	50 ft	100 ft	200 ft	500 ft	1000 ft
17	4 ft ø pile driving @ P12/P23 without BMPs	163.3	149.5	143.6	134.4	129.0	120.9	115.6
18	6 ft ø pile driving @ P27/P48 without BMPs	171.4	160.0	152.0	142.5	140.3	137.1	128.6
20	10 ft ø pile driving @ P24/P44 without BMPs	177.8	175.1	167.1	156.5	149.0	147.8	142.3

5. Discussion

5.1. Sound Propagation in the River Environment

In Tappan Zee Reach the riverbed bathymetry and sub-bottom properties are the most important environmental factors governing propagation of sound from pile driving activities, because the dominant acoustic wavelengths are comparable in scale to the water depth. For example the acoustic wavelength of the 125 Hz band where sound levels from the 8-10 ft piles are highest (Figure 7) is approximately 40 ft (Equation 2). In shallow water, sound is continually reflected and absorbed by the river bottom as it propagates away from the source. At long ranges the absorption of sound energy into the riverbed (called "bottom loss") becomes the primary attenuating mechanism. The bathymetric profile of the riverbed causes sound to propagate further along the deeper central channel than in the shallows to the east and west, resulting in sound level isopleths having a greater extent in the north-south direction.

The geoacoustic properties of the riverbed play an equally important role in influencing sound propagation in this environment. Whether the riverbed is absorptive or reflective depends upon the impedance contrast between the water and the substrate. Acoustic impedance is related to the density and speed of sound of a medium. If the impedance contrast between the water and the riverbed is low (i.e., if the densities and sound speeds are similar) then the riverbed is more absorptive. In the case of Tappan Zee Reach, the top sediment layer at the riverbed interface is composed of fine, water-saturated sediments (silty-clay) which have a relatively low impedance contrast with water. A rocky bottom, by contrast, would have a much higher impedance contrast than fine sediments and be more acoustically reflective. Propagation loss is generally higher over softer, more porous substrates.

The stratification of the riverbed sediments determines how bottom loss varies with frequency. Propagating sound waves in the water medium are coupled to the underlying sediments as they impinge onto the riverbed. The extent to which this coupling occurs is related to wavelength. Lower frequencies are coupled to deeper sediments, whereas higher frequencies are coupled to shallower sediments. Deeper sediments generally possess higher sound speeds, which can cause reflection (or refraction) of low frequencies back into the water column. On the other hand, volumetric absorption of acoustic energy is also much higher in sediments than in water; sound frequencies that are strongly coupled to the bottom, therefore, also tend to experience higher propagation loss (resulting in so called "leaky modes"). Finally, interference between reflections

from multiple sediment layers can both enhance and suppress certain frequencies. Due to these competing effects, bottom loss is a complex phenomenon that often goes against intuition.

An example of the strong influence of geoacoustics in the modeling of sound propagation in Tappan Zee Reach is the notch near 1 kHz observed in the PSD levels at long ranges (see Figure 32 and Figure 33). The notch corresponds to the transition from strongly bottom coupled sound propagation at low frequencies to weakly bottom coupled (i.e., primarily waterborne) sound propagation at higher frequencies. In this case, the mid-frequencies (0.3-2 kHz) are absorbed by the riverbed more strongly than the low frequencies (< 0.3 kHz) because sediment absorption increases with frequency; at higher frequencies (> 2 kHz), however, the sound energy is not strongly coupled to the riverbed and so bottom absorption becomes negligible. These competing mechanisms result in the model predicted notch in the PSD levels in the middle frequency range.

Another example of the influence of geoacoustics can be observed at short ranges, in the near-field peak level modeling. For the unmitigated piling (Figure 26), SPLs at distances between 200 ft and 480 ft rise to higher values for the 6 ft diameter pile (at P27/P48) than for the 8 ft diameter pile (at P20/P38). The cause for this phenomenon can be found in the markedly different thickness of the top sediment layer at the two locations, 25 ft and 85 ft respectively (see Table 4). In both cases sound is reflected from the interface between the first two sediment layers; at P27/P48, however, the condition of "critical reflection" (whereby sound is totally reflected at the interface for shallow angles of incidence) occurs at shorter range because of the thinner top sediment layer. The SPL, therefore, begins surging with range due to the onset of critical reflection at a distance of about 130 ft for the 6 ft pile compared to 300 ft for the 8 ft pile, causing the localized crossover. The same effect is not observed for the mitigated piling (Figure 27) due to the dominance of low frequencies (less attenuated by the bubble curtain) that do not "see" the shallow sediment layers.

As the previous case analyses have shown, the results of the sound propagation modeling are very sensitive to both the bathymetry and geoacoustic properties of the riverbed in Tappan Zee Reach. Precise, high-resolution bathymetric survey data are available for the Hudson River; the modeling uncertainty related to inaccuracies in bathymetry is therefore small. The uncertainty in model results associated with the geoacoustic properties of the riverbed, on the other hand, is more significant due to the fact that the acoustic properties of the riverbed sediments have not been directly measured at Tappan Zee Reach. The current study has presented a justifiable estimate of the sediment geoacoustic profiles based on available sediment stratigraphy from core samples and historical data for similar sediments. Nonetheless, a more rigorous estimation of the acoustic properties of the riverbed (either directly from coring studies or indirectly from transmission loss measurements) would significantly reduce uncertainty in the model estimates.

5.2. Pile Driving Sound Levels

The acoustic footprint of a single pile driving strike depends primarily on the following factors:

1. the energy and type of pile driving hammer,
2. the size and type of the pile, and
3. the water depth and substrate in which the pile is being driven.

The acoustic energy radiated into the aquatic environment by a struck pile is directly correlated to the kinetic energy that the impact hammer imparts to it. Engineering considerations about pile

penetration and load bearing capacity dictate that the impact hammer energy must be matched to the pile and to the resistance of the underlying soils (Parola, 1970). Greater hammer energy is generally required for larger diameter piles to achieve the desired load bearing capacity. The hammer energy must also be sufficient to overcome the local resistance of any substrate into which the pile is being driven. It is clear therefore that pile driving energy is largely imposed by the foundation load bearing requirements and cannot be arbitrarily reduced to shrink the acoustic footprint of pile driving operations.

The acoustic coupling between the pile and the water column is strongly influenced by the water depth at the piling location. In deep water, more of the pile is in contact with the water column and therefore more sound energy is injected directly into the aquatic environment. Furthermore, propagation loss is higher at shallow locations because more sound energy emanating from the pile is absorbed into the substrate. As a result, modeled footprints of SPL and single-strike SEL at Tappan Zee Reach were proportionately larger for piles driven in the deeper water of the river channel than on the shoals.

Source levels for the current study were based on published acoustic measurements of sound emission from impact driving of cylindrical steel piles in several projects (Table 2). Analysis of published pile driving data indicated that large diameter piles emit more sound energy at low frequencies than smaller piles (Figure 7). This is consistent with the physical expectation that larger structures should acoustically resonate at longer wavelengths (i.e., at lower frequencies). Modeled frequency spectra showed that in the Tappan Zee Reach environment 4-6 ft piles were subject to higher long range propagation loss than 8-10 ft piles because mid-frequencies were more strongly attenuated than low frequencies (see results in Appendix D).

5.3. Cumulative Sound Exposure

In addition to the source properties discussed in the previous section, cSEL footprints for the cumulative scenarios were influenced by the following two factors:

1. The number of pile driving strikes, and
2. The spatial distribution of the piling activity.

If a constant rate of hammering is assumed, then the number of pile driving strikes increases linearly with time. The cSEL, however, increases logarithmically in decibels with number of strikes (Equation 12). For example, the dB increase in cSEL during the first 10 minutes of pile driving is roughly equivalent to the dB increase in cSEL over the following two hours (assuming the activity is not disrupted). Similarly, driving two identical piles at the same site will always increase the total cSEL by 3 dB relative to a single pile, no matter the time required to install the piles. Pile driving at two separate locations, on the other hand, has a greater influence on the aggregate cSEL footprint than installing multiple piles at a single location. Footprints are larger for distributed operations because contours from different locations ensonify a greater total area for the same amount of activity.

The results from modeling of cumulative scenarios represent the total cSEL for a stationary receiver exposed to piling noise from multiple sites, regardless of whether these piles are being driven at the same time or in sequence. The only relevant assumption is that all the pile driving happens within a short enough time that the subject will not have started to recover from any temporary impact from the noise exposure. This is likely a very conservative assumption when the piling happens intermittently over an 8 hour work day. Another important consideration

regarding cumulative scenarios is that when piles from different piers are driven simultaneously it can readily be assumed that the sources are sufficiently uncorrelated and the noise sufficiently broadband that no coherent summing of individual pulses can ever take place.

5.4. Factors Influencing BMP Attenuation

As discussed in Section 3.3, while confined air-bubble curtains likely represent the best available technology for mitigating pile driving noise in Tappan Zee Reach, the quantitative effectiveness of this management practice reported in the literature is highly variable. Several factors are thought to influence the performance of confined air-bubble curtain systems:

1. Whether the bubble plume completely encloses the pile
2. The nature of the confinement barrier
3. The volume fraction of air inside the bubble plume
4. The performance of air compressors, hoses, and manifolds, and nozzles

The pile must be completely enclosed by bubbles in order to achieve maximum attenuation. If the coverage is incomplete, sound will escape from holes in the bubble curtain (Vagle, 2003). Confined bubble curtain systems specifically prevent the river flow from dispersing the bubble plume around the pile; full and consistent coverage may nonetheless be difficult to achieve when the riverbed is uneven or sloped, since the base of the curtain cannot sit flush on the riverbed.

Past projects have used both light fabric barriers and heavy rigid shells (such as steel pipes) to confine the bubble plume. Rigid shells hold up better to strong currents, but require heavy lifting machinery to deploy and recover. Light fabric barriers may be buffeted by currents and on occasion the bubbles plume itself may lift a fabric curtain off the base of the pile (CALTRANS, 2001). In general practice rigid shells are mostly found preferable; in addition a rigid barrier can be engineered to enhance noise attenuation by coating it with sound absorbing material or by incorporating an air space between concentric walls (MacGillivray et al., 2006).

Bubble curtains achieve sound attenuation by introducing a highly compressible fluid layer between the pile and the water column (Hannay, 2008). Increasing the air volume fraction inside the barrier creates a larger impedance mismatch at the pile wall, thereby better decoupling the pile from the water column. If insufficient air is injected into the confined volume between the barrier and the pile wall, the mitigation will be ineffective.

Adequate air injection and bubble plume confinement both depend critically on the design and construction of the bubble curtain, which must be tested under realistic conditions to verify its effectiveness. Hoses, manifolds, nozzles and compressors must continuously supply a sufficient amount of air to the system for it to be effective. Furthermore, an air bubble curtain system must be reasonably easy to set up at the job site or it may be deployed improperly by the construction contractor thus compromising its efficacy.

A review of published measurements of bubble curtain attenuation showed that performance at low frequencies, below 100 Hz, was poorer than at higher frequencies (Figure 10). Because the peak SPL metric is influenced primarily by high frequencies, air bubble curtains tend to be most effective at reducing peak levels close to the pile (Figure 27). At long ranges, however, the effectiveness of bubble curtains may be less. The modeling performed in this study has shown that high frequencies become spread out at longer propagation ranges, causing long-range SPLs

to depended more strongly on the low frequencies which are less attenuated by air-bubble curtains. In the modeling results BMPs were observed to be less effective at attenuating SPLs from pile driving at ranges longer than 10,000 ft (Figure 31).

6. Summary and Conclusions

This report has presented results from a noise modeling study carried out in support of the Tappan Zee/I-287 Corridor Project Environmental Impact Statement. This study used three different numerical sound propagation models to estimate underwater noise levels that would be produced by impact pile driving activities associated with construction of the proposed bridge in Tappan Zee Reach. The acoustic models used wave-equation based algorithms (parabolic equation and wavenumber integration) to simulate sound propagation in the Hudson River environment, accounting for the frequency composition of the source signal and the acoustic properties of the water column and riverbed substrates. Sound propagation was modeled in three dimensions (range, depth and azimuth) at ranges up to 50,000 ft from the proposed bridge.

Use of three sound propagation models with complementary features and realms of applicability allowed for efficient modeling of sound propagation in multiple domains (near-field, far-field, time-domain, and frequency-domain). This was a necessity in order to be able to compute five different sound level metrics required for the noise impact assessment (SEL, cSEL, *rms* SPL, peak SPL, and particle velocity). Near-field metrics (peak SPL and particle velocity) were modeled using a time-domain wavenumber integration model (VSTACK) that was valid at short range from the piles. The wavenumber integration model simulated the pile as a vertically distributed source, taking into account the acoustic contribution of pile segments in the water and in the substrate. Far-field energy metrics (SEL, cSEL) were modeled using a frequency-domain parabolic equation model (MONM) that was able to account for three-dimensional bathymetry variations and range-dependent environmental parameters. Pulse lengths were computed using a time-domain PE model (FWRAM) in order to derive *rms* SPL results from the SEL modeling. The longer range modeling neglected the distributed nature of the pile in computing propagation loss, which is a valid assumption in the far-field zone where the acoustic radiation from the pile is indistinguishable from that of a point-source. Power spectral density levels for the pile driving were computed from the frequency resolved *rms* SPL model results.

Impact pile driving source levels in 1/3-octave bands were derived via back-propagation of published measurements for piles > 3 ft diameter. An ensemble of reported measurements, obtained at different locations and distances, were averaged in order to reduce uncertainty associated with the back-propagation. The source level estimates included corrections to adjust for pile diameter and hammer energy. Furthermore, different frequency distributions were derived for 8-10 ft diameter and 4-6 ft diameter piles since the published data showed that larger piles produced proportionately higher low frequency sound energy than smaller piles. Time-domain source levels were derived from spectral factorization of the 1/3-octave band source levels, which is expected to produce conservative estimates of SPLs from pile driving.

Environmental models of bathymetry, geoacoustics profiles, and water sound speed profiles were used as input to the acoustic propagation models. Water depths for the Hudson River were derived from high resolution bathymetry mapping survey data. The sound speed in water was

estimated based on temperature and salinity measurements for the month of October. October conditions were selected as representative for the modeling, because of the prominent lack of stratification in the water column, yielding a uniform profile that was expected to best represent average sound propagation conditions in Tappan Zee Reach. Geoacoustic profiles were derived from sediment stratigraphy data underneath the bridge span. Five distinct sedimentary units were identified in the stratigraphy cross-sections. For each of these sediment units, the acoustic properties were estimated based on the classification of the component soils. Eight different geoacoustic profiles were derived, one for each unique source location along the bridge span, plus an average profile used for long-range modeling.

Confined air bubble curtains were identified as the likely best BMP strategy for mitigating pile driving noise in Tappan Zee Reach. Published measurements were collected and analyzed to estimate a mean frequency attenuation curve for confined air bubble curtain systems. A review of the available data indicated that these systems have best performance at frequencies above 100 Hz, although the total broadband attenuation varied considerably between studies. Strong currents and variable water depths are present in Tappan Zee Reach, which could influence bubble curtain performance. In accordance with assessment guidelines published by WSDOT and CALTRANS, the assumed broadband BMP attenuation (at the source) was limited to 10 dB in the modeling. While some studies have reported higher broadband attenuation values, this is believed to be a realistic BMP performance target for the proposed construction project.

While model results were computed in three spatial dimensions, sound levels were reduced to two-dimensional contours for presentation by taking the maximum sound level over all depths at each receiver location. This approach is conservative, as it makes no assumption as to the depth where an organism is present in the water column.

Bathymetry was found to have a large influence on modeled sound levels in Tappan Zee Reach because sound absorption into the bottom, and therefore transmission loss, is much greater in shallow water. Pile driving isopleths extended significantly further along the central channel than along the east and west shoals; as a result, the contours were often asymmetrical around the piles. Similarly, propagation loss was much lower for piles driven in the central channel than for piles driven on the shoals. This tended to enhance levels from the largest piles located in the central channel. Furthermore, frequency dependent propagation effects tended to attenuate levels from 4-6 ft piles at shorter ranges than levels from 8-10 ft piles due to their different frequency composition.

Application of BMPs was found to significantly reduce pile driving sound levels, although BMPs were more effective in the near-field, due to frequency dependent propagation effects. For the cumulative scenarios, cSEL contour areas without BMPs at the 197 dB re 1 $\mu Pa^2 \cdot s$ threshold level ranged from 4,100 to 53,000 thousands of ft^2. cSEL contour areas with BMPs at the 197 dB re 1 $\mu Pa^2 \cdot s$ threshold level ranged from 180 to 30,000 thousands of ft^2. Cumulative sound levels were not appreciably different between scenarios representing the two different bridge design options. For the single-strike scenarios, unmitigated peak SPLs at the 208 dB re 1 µPa threshold level ranged from 43-861 ft. Mitigated peak SPLs ranged from 26-247 ft.

7. References

Arup, 2010. Foundation drawing: Single / dual level bridge Tappan Zee Bridge. Technical drawings B-4342 and B-4343 prepared by Arup for NYSDOT.

CALTRANS, 2001. San Francisco–Oakland Bay Bridge east span seismic safety project, pile installation demonstration project. Marine mammal impact assessment. PIDP EA 012081, PIDP 04-ALA-80-0.0/0.5, Caltrans Contract 04A0148, Task Order 205.10.90.

CALTRANS, 2009. Technical guidance for assessment and mitigation of the hydroacoustic effects of pile driving on Fish. Technical report prepared by ICF Jones & Stokes and Illingworth and Rodkin, Inc, for California Department of Transportation, Sacramento CA.

Claerbout, J. F., 1976. Fundamentals of Geophysical Data Processing: McGraw-Hill Book Co.

Collins, M.D. 1993. A split-step Pade solution for the parabolic equation method. Journal of the Acoustical Society of America. 93(4), 1736-1742.

Coppens, A. B., 1981. Simple equations for the speed of sound in Neptunian waters. Journal of the Acoustical Society of America. 69(3), 862-863.

Fahy, F. J., 1977. Measurement of acoustic intensity using the cross-spectral density of two microphone signals. Journal of the Acoustical Society of America. 62, 1057–1059.

Hamilton, E. L., 1980. Geoacoustic modeling of the sea floor, Journal of the Acoustical Society of America., 68(5), 1313–1340.

Hannay, D., and Racca, R., 2005. Acoustic Model Validation. Technical report prepared for Sakhalin Energy Investment Company by JASCO Research Ltd. Document Number 0000-S-90-04-T-7006-00-E.

Hannay, D., 2008. Modeling of acoustic attenuation of an air curtain. Appendix B. in Ayers, R., Jones, W., and Hannay, D., Methods to reduce lateral noise propagation from seismic exploration vessels. Technical report M07RS13346 prepared for Minerals Management Service, U.S. Department of Interior.

Illingworth and Rodkin, Inc. 2006. Letter to Bill Cooke (Manson Construction Co.) reporting results of underwater sound measurements – Impact Driving of 40- and 30-Inch Steel Piles. August 14.

Jensen, F., Kuperman, W., Porter, B., and Schmidt, H., 2000. Computational Ocean Acoustics. Springer-Verlag, New York.

Lacey, H. S., 2008. Tappan Zee Bridge/I-287 Corridor alternatives analysis / environmental assessment / environmental impact statement: Geotechnical data report (draft). Technical report prepared by Mueser Rutledge Consulting Engineers for New York State Thruway Authority.

MacGillivray, A., and Racca, R., 2005. Sound pressure and particle velocity measurement from marine pile driving at Eagle Harbor maintenance facility, Bainbridge Island WA. Technical report prepared by JASCO Research Ltd. for Washington State Department of Transportation.

MacGillivray, A., Ziegler, E., and Laughlin, J., 2006. Underwater acoustic measurements from Washington State Ferries 2006 Mukilteo Ferry Terminal Test Pile Project. Technical report prepared by JASCO Research Ltd. for Washington State Ferries and Washington State Department of Transportation.

McKenzie-Maxon, C., 2000. Offshore wind-turbine construction offshore pile-driving underwater and above-water noise measurements and analysis. Odegaard & Danneskiold Samsoe A/S Technical report No. 00.877 Copenhagen, Denmark.

Nehls, G., Betke, K., Eckelmann, S. and Ros. M., 2007. Assessment and costs of potential engineering solutions for the mitigation of the impacts of underwater noise arising from the construction of offshore windfarms. Technical report prepared by BioConsult SH report, Husum, Germany for COWRIE.

OSI, 2009. Final Report – Salinity, Turbidity & Suspended Solids Concentration Study: Tappan Zee Bridge / I-287 Project. Technical report prepared for Earth Tech AECOM by Ocean Surveys, Inc. OSI Report No. 08ES085.

Parola, J. F., 1970. Mechanics of impact pile driving. Thesis dissertation, University of Illinois.

Racca, R., MacGillivray, A., and Laurinolli, M., 2007. NaiKun meteo mast installation: Underwater sound level monitoring of pile driving operations. Technical report prepared for NaiKun Wind Development by JASCO Research Ltd.

Reyff, J. A., 2003. Underwater sound levels associated with seismic retrofit construction of the Richmond-San Rafael Bridge - Measurements results for the driving of temporary and permanent piles. Technical report prepared by Illingworth and Rodkin, Inc. for California Department of Transportation.

Robinson, S., Lepper, P., Ablitt, J., 2007. Measurement of the underwater radiated noise from marine piling including characterisation of a "soft start" period. Proceedings of IEEE Oceans, 2007.

Schultz-von Glahn M, Betke K, Nehls G., 2006. Underwater noise reduction of pile driving for offshore wind turbines – Evaluation of several techniques under offshore conditions. UFOPLAN Ref. No. 205 53 113, final report. The Federal Environment Agency (Umweltbundesamt UBA), Berlin.

Vagle, S., 2003. On the impact of underwater pile-driving noise on marine life. Technical report prepared by Institute of Ocean Sciences, DFO/Pacific, Ocean Science and Productivity Division.

WSDOT, 2010a. Underwater sound levels associated with driving steel piles for the State Route 520 bridge replacement and HOV project pile installation test program. Technical report prepared by Illingworth and Rodkin Inc. for Washington State Department of Transportation, Seattle WA.

WSDOT, 2010b. Biological Assessment Preparation Advanced Training Manual. Technical report prepared by Washington State Department of Transportation, Seattle WA.

Zhang, Y., and Tindle, C., 1995. Improved equivalent fluid approximations for a low shear speed ocean bottom. Journal of the Acoustical Society of America, 98(6), 3391-3396.